

Optimal Design Framework for Distributed Array Using Magnetically-Actuated Satellite Swarm

Seang Shim, Yuta Takahashi, *Student Member, IEEE*, Naoto Usami, *Member, IEEE*, and Shin-ichiro Sakai

Abstract—Distributed space antennas using electromagnetic formation flight (EMFF) are a promising architecture for large-aperture, long-life space communication systems. Their feasible aperture, however, is governed by coupled constraints on antenna performance, satellite mass, power generation, coil geometry, and formation-keeping power. This paper proposes a system-level design framework for EMFF-based distributed space antennas. It links phased-array requirements with satellite-level sizing constraints and provides a static grid-based reference for designing feasible apertures under a fixed system mass. Unlike our previous bucket-brigade disturbance-compensation model, the formation-maintenance requirement is incorporated through a control index derived from distributed-control simulations. This index is integrated into an antenna-aperture maximization problem with sizing, power, coil, and sidelobe-envelope constraints. Parametric case studies examine margin magnetic moment, prescribed transmit power, and large inter-satellite spacing. Results show that increasing system mass improves footprint reduction or effective isotropic radiated power only while satellite-level design headroom remains. In direct-to-device cases with 0.15-m spacing, generated-power and coil-geometry constraints dominate the feasible aperture. In the 0.60-m large-spacing case, the required coil burden can exceed satellite-level mass, size, and power capacities, making the design infeasible despite favorable communication performance. The proposed framework enables the design and evaluation of feasible static grid-based EMFF distributed antennas under coupled antenna, satellite, and control constraints.

Index Terms—Distributed space antennas, electromagnetic formation flight, non-terrestrial networks.

I. INTRODUCTION

DISTRIBUTED space antennas composed of palm-sized satellites provide a scalable architecture for high-performance communication systems under fuel-free formation maintenance, such as electromagnetic formation flight (EMFF). Previous space antennas typically required narrow beams to suppress interference with other beams [4] and high-gain transmission over long distances, which in turn required larger antenna structures through increased element counts or inter-element spacing [5], [6]. Examples include deep-space antennas [7], ground terminals with tiny receivers [8], and space membrane antennas [9]. Compared with monolithic antennas, distributed architectures alleviate single-point

Seang Shim and Yuta Takahashi contributed equally as co-first authors. This work was supported by JST SPRING, Japan Grant Number JPMJSP2104.

S. Shim is with The Graduate University for Advanced Studies, Sagamihara, Kanagawa 252-5210, Japan.

Y. Takahashi is with Institute of Science Tokyo, Tokyo 152-8550, Japan, and Interstellar Technologies Inc., Hiroo, Hokkaido 089-2113, Japan.

N. Usami and S.-i. Sakai are with Japan Aerospace Exploration Agency, Sagamihara, Kanagawa 252-5210, Japan.

Corresponding author: Seang Shim (e-mail: shim.seang@ac.jaxa.jp).

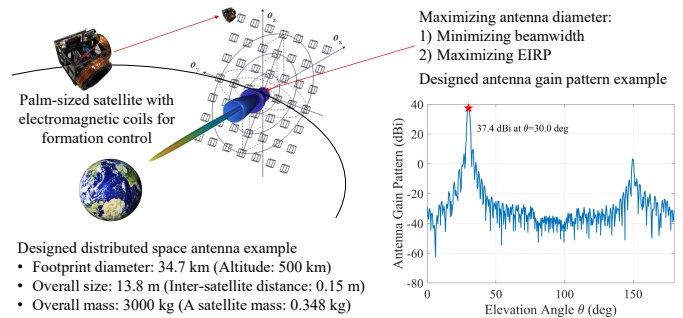


Fig. 1. Overview of design optimization of distributed space antennas for the trade-off between formation control and antenna performance. The magnetic coils in each satellite generate magnetic fields, and their interactions enable long-term formation maintenance. Detailed guidance and control frameworks are provided in our previous studies [1]–[3].

failures, payload-size limitations, and cost escalation while enabling large effective apertures [1], [7], [10]–[15]. Their practical realization, however, requires active position control to preserve the formation against orbital disturbances such as the J_2 effect [16]. Without such control, antenna performance deteriorates over time: excessive intersatellite spacing induces grating lobes, whereas insufficient spacing increases mutual coupling [5], [6], [17]. Because the propulsion required for formation maintenance directly affects mission lifetime, fuel-free control is of particular interest.

EMFF provides a physically attractive solution to this requirement. By exploiting magnetic torquers (MTQs), which are standard actuators on small satellites, EMFF enables simultaneous control of relative positions and absolute attitudes [1], [13], [14], [18], [19]. Electromagnetic formation control using alternating current (AC) has also been studied with learning-based control [3], [20]. Prior studies have established exact interaction models based on the Biot–Savart law [21], learning-based approximations [22], and dipole approximations for far-field applications [18]. In addition, the Earth’s magnetic field can be exploited to regulate the angular momentum of the overall system and mitigate unnecessary interference [14]. Alternative fuel-free approaches, such as differential drag and tethers [23], [24], are less suitable for distributed space antennas because the former is strongly attitude-dependent, whereas the latter lacks scalability and reconfigurability [25]. Existing EMFF studies have largely focused on small numbers of satellites [13], whereas practical distributed space antennas may require substantially larger arrays [8]. The distributed architecture becomes attractive precisely in this large-scale regime, where monolithic systems are constrained by payload,

cost, and reliability considerations [12]. In general, a large array size improves communication performance and enables a narrow beam to prevent interference with other communication areas. However, the electromagnetic force decays with the fourth power of the distance. This distance-dependent limit directly limits the inter-satellite distance for a given power consumption. Therefore, it is important to clarify the trade-off between control and antenna performance with respect to distance.

Despite these advantages, the system-level potential of EMFF-based distributed antennas remains unclear. A previous study clarified that magnetically actuated satellite swarms can improve power efficiency as the number of satellites increases when constructing large-scale distributed space structures, using a convex-optimization-based formation-keeping power analysis [26]. Although the convex-optimization-based framework is suitable for evaluating the overall system and per-satellite power trends, this framework is unsuitable for detailed component-level satellite design due to conservative worst-case specifications. This motivates a system-level feasibility analysis that jointly accounts for communication metrics, including sidelobe levels and effective isotropic radiated power (EIRP), and the control power required for deployment and long-term formation maintenance [27].

To address this need, this paper presents an extended system-level design methodology for EMFF-based distributed space antennas that meets prescribed antenna performance requirements while enabling practical satellite sizing. This paper builds on our previous work on the feasibility study of EMFF-based distributed space antennas [28]. In that study, the formation-maintenance requirement was derived using a bucket-brigade compensation model for a grid formation. Although this model provided an analytically tractable first estimate of the required magnetic moment and control power, it relied on an idealized compensation structure and did not directly reflect the behavior of distributed formation control. In contrast, this paper estimates the required magnetic moment and control power from numerical simulations of distributed formation control, thereby providing a more realistic basis for system-level sizing.

The remainder of this paper is organized as follows. Section II reviews the underlying orbital dynamics, magnetic interaction model, and planar phased-array antenna formulation. Our problem formulation is presented in Section III to define the variables describing the distributed antenna. As a main result, Section IV presents a nonconvex optimization-based framework for designing distributed space antennas, subject to satellite-level mass and power constraints, as well as antenna performance and formation-maintenance constraints for grid-based distributed antennas. Section V presents the numerical case studies based on the integrated optimization framework. Section VI concludes the paper. Throughout the paper, perfect knowledge of all satellite states is assumed in order to focus on trend analysis.

II. PRELIMINARIES

This section summarizes the control of the relative distance from J_2 disturbance using EMFF and the derivation of the

antenna performance, focusing on the EIRP and beamwidth.

A. Linearized/Averaged Relative Orbital Dynamics

We introduce the approximated dynamics of relative orbital motion under J_2 disturbances [16]. Let $P_j = [r_{\text{ref}} + x_j; y_j; z_j]$ be the position vector of the j -th satellite from the center of the Earth in the local vertical, local horizontal (LVLH) coordinate frame, where r_{ref} is the constant orbital radius of the reference orbit. We obtain $\dot{P}_j = \nabla U_{J_2}$ where $\nabla U_{J_2} \in \mathbb{R}^3$ is the gravity gradient associated with its orbital dynamics [16]:

$$\nabla U_{J_2}(P_j, i, \theta) = - \begin{bmatrix} \frac{\mu_g}{\|P_j\|^2} \\ 0 \\ 0 \end{bmatrix} - \frac{k_{J_2}}{\|P_j\|^4} \begin{bmatrix} 1 - 3 \sin^2 i \sin^2 \theta \\ \sin^2 i \sin 2\theta \\ \sin 2i \sin \theta \end{bmatrix}, \quad (1)$$

where the constant μ_g , the inclination i , the argument of latitude θ , and J_2 coefficient $k_{J_2} = 2.63e^{10} \text{ km}^5/\text{s}^2$. A previous study defined a reference orbit to compensate J_2 effect:

$$\omega_{\text{ref}} = \begin{bmatrix} 0 \\ 0 \\ c_+ \omega_o \end{bmatrix} \text{ s.t. } \omega_{\text{ref}} \times \omega_{\text{ref}} \times r_{\text{ref}} = \int_0^{2\pi} \nabla U_{J_2}(\theta) \frac{d\theta}{2\pi},$$

$$\omega_o = \sqrt{\frac{\mu_g}{r_{\text{ref}}^3}}, \quad c_{\pm} = \sqrt{1 \pm s_{J_2}}, \quad s_{J_2} = \frac{k_{J_2}(1 + 3 \cos 2i_{\text{ref}})}{4\mu_g r_{\text{ref}}^2}. \quad (2)$$

We include an additional compensation term for the separation of the orbital planes owing to the time-varying longitudes of the ascending nodes $\Omega(t)$ such that $\theta(t) = \omega_{z\text{ref}} t$ where

$$\omega_{z\text{ref}} = c_+ \omega - \dot{\Omega}_{\text{avg}j} \cos i_j = \omega_o \left(c_+ + \frac{k_{J_2} \cos^2 i}{\mu r_{\text{ref}}^2} \right), \quad (3)$$

where $\dot{\Omega}(\theta) = -2k_{J_2} \cos i \sin^2 \theta / (\|\mathbf{h}\| r_{\text{ref}}^3)$, $|\dot{\Omega}_{\text{avg}}| = |\int_0^{2\pi} \dot{\Omega}(\theta) d\theta / 2\pi| \lesssim 2e^{-6} \cos i_{\text{ref}}$ under $i_j \approx i_k$ [1], [29].

Linearization based on the reference orbit is used to derive the relative motion between two satellites. Let $r_{jk} = r_j - r_k = [x_{jk}; y_{jk}; z_{jk}]$ be the relative position from the k -th satellite to the j -th one. The dynamics of the linearized relative motion around the reference orbit in the LVLH frame are [1], [29]

$$\begin{aligned} \ddot{\bar{x}} - 2\omega_{xy} \dot{\bar{y}} - 3\omega_{xy}^2 \bar{x} - \frac{4\omega_{xy}^2}{c_-^2/s_{J_2}} \left(2\bar{x} + \frac{\dot{\bar{y}}}{\omega_{xy}} \right) &= c_+(u_x + d_x) \\ \ddot{\bar{y}} + 2\omega_{xy} \dot{\bar{x}} &= c_-(u_y + d_y) \\ \ddot{z} + \omega_z^2 z &= 2l\omega_z \cos(\omega_z t + \theta_z) + (u_z + d_z) \\ \begin{cases} \bar{x} = c_+ x, & \bar{y} = c_- y, & \omega_{xy} = c_- \omega_o, \\ \omega_z = \omega_{z\text{ref}} + f_1(\delta\dot{\Omega}_{\text{avg}}) \approx \omega_{z\text{ref}}, & r_z \sin \theta_z = z, \\ l \sin \theta_z + \omega_z r_z \cos \theta_z = \dot{z}, \end{cases} \end{aligned} \quad (4)$$

where the subscript jk will be omitted, $l(\delta\dot{\Omega}_{\text{avg}jk}) = -r_{\text{ref}} \sin i_j \sin i_k f_2(\delta\dot{\Omega}_{\text{avg}jk})$, and the dynamics along the z -axis include a term for compensating for errors in the cross-track motion owing to time averaging. Assuming that the satellites have identical i , the amplitude of the relative orbital motion along the z -axis reaches a constant value, which means that $l(\delta\dot{\Omega}_{\text{avg}}) \approx 0$ in (4).

B. Averaged J_2 Relative Orbital Parameters

We derive the orbital indices, averaged J_2 relative orbital parameters, and this denotes desired stable trajectories $p_d(t)$. An analytical solution of (4) is [1], [29]:

$$\begin{bmatrix} x(t) \\ y(t) \\ z(t) \end{bmatrix} = \begin{bmatrix} r_o(0, t) \\ 0 \\ 0 \end{bmatrix} + \begin{bmatrix} r_{xy} \sin(\omega_{xy}t + \theta_{xy})/c_+ \\ 2r_{xy} \cos(\omega_{xy}t + \theta_{xy})/c_- \\ (r_z + lt) \sin(\omega_z t + \theta_z) \end{bmatrix}, \quad (5)$$

$$r_o(0, t) = [2C_1 \quad C_4 - \epsilon_2 C_1 t]^\top, \quad \epsilon_2 = \frac{3 + 5sJ_2}{c_+ c_-} \omega_{xy},$$

where $r_o(0, t) \in \mathbb{R}^2$ represents the center position of the relative orbit at time t , $l(\delta\dot{\Omega}_{avgjk}) \approx 0$, where $f_{1,2} \in \mathbb{R}$ is a function of $\delta\Omega_{jk0}$. The orbital indices calculated at the estimation time ($t = 0$) are specified as [1]

$$\begin{cases} C_1 = c_+/c_-^2(2\bar{x} + \dot{\bar{y}}/\omega_{xy}), & C_4 = (\bar{y} - 2\dot{\bar{x}}/\omega_{xy})/c_- \\ r_{xy}^2 = C_2^2 + C_3^2, & \theta_{xy} = \tan^{-1}(C_3, C_2) \\ C_2 = (\bar{y} - c_- C_4)/2, & C_3 = \bar{x} - 2c_+ C_1 \\ r_z^2 = C_6^2 + C_5^2, & \theta_z = \tan^{-1}(C_6, C_5) \\ C_5 = \dot{z}/\omega_z, & C_6 = z. \end{cases} \quad (6)$$

It is clear from (5) that the motions are governed by $r_{xy,z}$ and $\delta\theta = \theta_z - \theta_{xy}$, as defined in (6). A simple calculation yields the following relationship between $r_{xy,z}$, $\delta\theta$, and the satellite swarm angle (Θ_P, Θ_{z-xy}) for the aperture design:

$$r_z = \frac{r_{xy}}{\tan \Theta_P} \frac{\cos \Theta_{z-xy}}{\cos(\theta_z - \theta_{xy})}, \quad \theta_z = \theta_{xy} + \tan^{-1}(2 \tan \Theta_{z-xy}). \quad (7)$$

The desired trajectory along the z -axis is selected based on the x - y motion: $\omega_{zd} = \omega_{xy}$ and $\theta_{zd} = \theta_{xy} + \tan^{-1}(2 \tan \Theta_{z-xy})$. This derives the desired stable trajectories $p_d(t)$

$$p_d(t) = \begin{bmatrix} (1/c_+)r_{xy}d \sin(\omega_{xy}t + \theta_{xy}) \\ (1/c_-)2r_{xy}d \cos(\omega_{xy}t + \theta_{xy}) \\ \frac{r_{xy}d}{\tan \Theta_P} \frac{\cos(\Theta_{z-xy})}{\cos(\theta_z - \theta_{xy})} \sin(\omega_{xy}t + \theta_{zd}(\Theta_{z-xy}, t)) \end{bmatrix}. \quad (8)$$

Note that $\omega_{zd} = \omega_{xy}$ is realized via the z -axis orbit control to maintain the z -axis orbital frequency ω_z in ω_{xy} or it works with the disturbance $d_{fz} = (\omega_{xy}^2 - \omega_z^2)z$ on p_d [1], [29]:

$$d_{fz}(t) = r_{zd}(\omega_{xy}^2 \sin(\omega_{xy}t + \theta_z) - \omega_z^2 \sin(\omega_z t + \theta_z)). \quad (9)$$

C. Magnetic Interaction Approximation Model

This subsection introduces the approximation of the magnetic field interaction model. We define the magnetic moment $\boldsymbol{\mu}$ and the resistance of a single-axis coil R_{coil} as

$$\boldsymbol{\mu} = \pi N_t a_{\text{coil}}^2 c_{\text{coil}} \mathbf{n}, \quad R_{\text{coil}} = 2a_{\text{coil}} N_t p_c / r_{\text{coil}}^2, \quad (10)$$

where N_t is the number of coil turns, a_{coil} is the coil radius, c_{coil} is the coil current, \mathbf{n} is a vector normal to the coil plane, p_c is the wire resistivity, and r_{coil} is the wire radius. A previous study [20] simplified a dipole model approximation [18] as the bilinear polynomial formulation using the line-of-sight frame $\{\mathcal{LOS}_{j \leftarrow k}\}$ (see Definition 1). Then, the input exerted on the j -th agent by the k -th agent is :

$$u_{j \leftarrow k}^a = \begin{bmatrix} f_{j \leftarrow k}^a \\ \tau_{j \leftarrow k}^a \end{bmatrix} = \frac{\mu_0}{4\pi} Q_{j \leftarrow k}(r_{j \leftarrow k}) (\boldsymbol{\mu}_k^a \otimes \boldsymbol{\mu}_j^a), \quad (11)$$

where μ_0 is the permeability of free space, $\boldsymbol{\mu}_{j,k}$ are the magnetic moments of the j, k -th coils, $Q_{j \leftarrow k} \in \mathbb{R}^{6 \times 9}$ is [20]

$$Q_{j \leftarrow k} = (I_2 \otimes C^{A/L_{j \leftarrow k}}) \begin{bmatrix} \Psi_f(r_{j \leftarrow k}) \\ \Psi_\tau(r_{j \leftarrow k}) \end{bmatrix} (C^{L_{j \leftarrow k}/A} \otimes C^{L_{j \leftarrow k}/A}),$$

and the vector from the k -th coil to the j -th coil $r_{j \leftarrow k}$ yields

$$\begin{cases} \Psi_f = \frac{1}{\|r_{j \leftarrow k}\|^4} \begin{bmatrix} -6 & 0 & 0 & 0 & 3 & 0 & 0 & 0 & 3 \\ 0 & 3 & 0 & 3 & 0 & 0 & 0 & 0 & 0 \\ 0 & 0 & 3 & 0 & 0 & 0 & 3 & 0 & 0 \end{bmatrix} \\ \Psi_\tau = \frac{1}{\|r_{j \leftarrow k}\|^3} \begin{bmatrix} 0 & 0 & 0 & 0 & 0 & 1 & 0 & -1 & 0 \\ 0 & 0 & 2 & 0 & 0 & 0 & 1 & 0 & 0 \\ 0 & -2 & 0 & -1 & 0 & 0 & 0 & 0 & 0 \end{bmatrix} \end{cases}.$$

Definition 1. The line-of-sight frame $\{\mathcal{LOS}_{j \leftarrow k}\}$ [20] is attached to the k -th agent and oriented toward the j -th agent. It is defined in (12), with the associated coordinate transformation matrix $C^{O/L_{j \leftarrow k}} \in \mathbb{R}^{3 \times 3}$ expressed as $C^{A/L_{j \leftarrow k}} = C(r_{j \leftarrow k}^a, f_{j \leftarrow k}^a \times r_{j \leftarrow k}^a)$ where we define the coordinate transformation matrix given the arbitrary vectors $v^a, w^a \in \mathbb{R}^3$:

$$\mathcal{C}(v^a, w^a) = \left[\mathbf{e}_x \triangleq \frac{v^a}{\|v^a\|}, \mathbf{e}_y \triangleq \frac{v^a \times w^a}{\|v^a \times w^a\|}, \mathbf{e}_z \triangleq \mathbf{e}_x \times \mathbf{e}_y \right]. \quad (12)$$

D. Optimal Electromagnetic Swarm Control

We consider the position and attitude control of multiple satellites using the magnetic interaction model defined in the previous subsection. We assume that the j -th magnetic moment is driven by a sinusoidal wave [20]:

$$\boldsymbol{\mu}_j(t) = \bar{\boldsymbol{\mu}}_j \sin(\omega_j t + \boldsymbol{\theta}_j) = \mathbf{s}_j \sin(\omega_j t) + \mathbf{c}_j \cos(\omega_j t), \quad (13)$$

where the amplitudes of the cosine and sine components are $\mathbf{s}_j \in \mathbb{R}^3$ and $\mathbf{c}_j \in \mathbb{R}^3$, respectively, and $\boldsymbol{\theta}_j \in \mathbb{R}^3$ are phases for the j -th MTQ. The first-order averaged input $\bar{u}_{j \leftarrow k} \in \mathbb{R}^6$ is

$$\bar{u}_{j \leftarrow k} = \frac{1}{2} \frac{\mu_0}{4\pi} Q_{j \leftarrow k} (\mathbf{s}_k^a \otimes \mathbf{s}_j^a + \mathbf{c}_k^a \otimes \mathbf{c}_j^a) \text{ if } \omega_j = \omega_k. \quad (14)$$

We formulate the power-optimal dipole allocation [20] as

$$\begin{aligned} \min \quad & J_p = \|[s_j^a; \mathbf{s}_k^a; \mathbf{c}_j^a; \mathbf{c}_k^a]\|^2 / 2 \\ \text{s.t.} \quad & \frac{\mu_0}{8\pi} Q_{j \leftarrow k} (\mathbf{s}_k^a \otimes \mathbf{s}_j^a + \mathbf{c}_k^a \otimes \mathbf{c}_j^a) = u_{j \leftarrow k}^a \end{aligned} \quad (15)$$

and its Lagrange dual problem of the problem in (15) is

$$\max_{\lambda \in \mathbb{R}^6} J_d = \frac{-\lambda^\top u_{j \leftarrow k}^a}{\mu_0 / (8\pi)} \quad \text{s.t.} \quad P_\lambda = \begin{bmatrix} E_3 & R_\lambda \\ R_\lambda^\top & E_3 \end{bmatrix} \succeq 0, \quad (16)$$

where the Lagrange multiplier vector $\lambda \in \mathbb{R}^6$ and $R_\lambda \in \mathbb{R}^{3 \times 3}$ satisfies $\text{vec}(R_\lambda) = Q_{j \leftarrow k}^\top \lambda$ [20]. Thus, the required magnetic dipole power magnitude for control can be derived using (16) [20] because the lower bound is obtained as $J_d \leq J_p$ [30] and $J_d = J_p$ for $n = 2$ [26].

E. Planar Phased-Array Antenna Formulation

This subsection introduces the effective isotropic radiated power (EIRP) for a planar phased-array antenna characterized by uniform element spacing, omnidirectional elements, and identical excitation amplitudes across all elements. The EIRP is the product of antenna gain G_T and the transmitting

power P_T [27], where P_T is the total of each element transmitting power P_t . Then, we obtain $EIRP = P_T G_T = (P_t N_{lx} N_{ly}) G_T$ where N_{lx} and N_{ly} are the number of satellites per grid side, respectively. Assuming that the antenna loss is negligible, G_T is equal to the maximum directivity \bar{D} [5]:

$$\bar{D} \triangleq \max_{\theta, \phi} D(\theta, \phi) = \max_{\theta, \phi} \frac{4\pi B(\theta, \phi)}{\int_0^{2\pi} \int_0^\pi B(\theta, \phi) \sin \theta d\theta d\phi}, \quad (17)$$

where θ and ϕ are the elevation and azimuth angles in the polar coordinate system, as shown in Fig. 2a. Here, $B(\theta, \phi)$ denotes the dimensionless normalized gain pattern, which is defined from the normalized field array factor $A(\theta, \phi)$ as

$$B(\theta, \phi) = |A(\theta, \phi)|^2. \quad (18)$$

For a rectangular planar array with uniform excitation, the normalized field array factor is expressed as the product of two linear-array factors [5]:

$$A(\theta, \phi) = A_x(u_x) A_y(u_y),$$

$$A_x(u_x) = \frac{1}{N_{lx}} \frac{\sin(N_{lx} u_x)}{\sin(u_x)}, \quad A_y(u_y) = \frac{1}{N_{ly}} \frac{\sin(N_{ly} u_y)}{\sin(u_y)}. \quad (19)$$

Here, u_x and u_y are defined as

$$u_x = kd_x (\sin \theta \cos \phi - \sin \theta_0 \cos \phi_0), \quad (20)$$

$$u_y = kd_y (\sin \theta \sin \phi - \sin \theta_0 \sin \phi_0),$$

where $k = \pi/\lambda$, λ is the wavelength, d_x and d_y are the element spacings along the two array axes, and (θ_0, ϕ_0) denotes the main-beam direction. When mutual coupling is neglected, averaging (17) over all directions gives the following approximation [31], [32]:

$$G_T = \bar{D} \approx N_l^2. \quad (21)$$

Finally, $N_l = N_{lx} = N_{ly}$ derives EIRP as follows:

$$EIRP_{\max} \triangleq P_T G_T = P_t N_l^4. \quad (22)$$

III. PROBLEM FORMULATION

1) *Grid Structure Array Model*: We primarily use a simplified model of a square phased array in Fig. (2) and the elements are equally spaced on a grid.

Assumption 1. We consider a distributed space antenna of a square phased array as shown in Fig. 2b, i.e.,

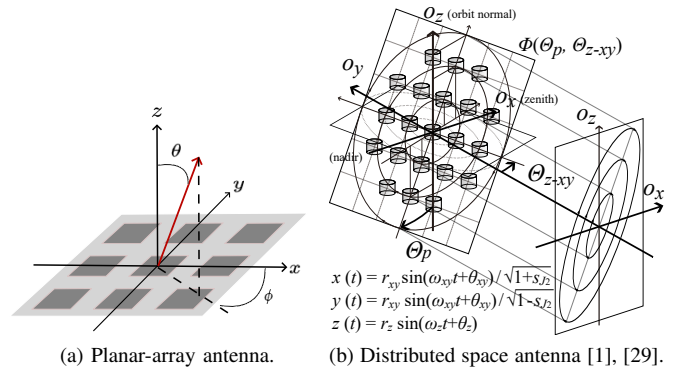
$$N_{\text{all}} \triangleq N_l^2 \triangleq (2n+1)^2, \quad (23)$$

where N_l is used for antenna context in subsection II-E. Its total system mass \bar{m}_{sys} , their inter-element distance d_{sat} , and associated total length r_l are user-defined constant values:

$$\bar{m}_{\text{sys}} \triangleq \text{const.}, \quad d_{\text{sat}} \triangleq \text{const.}, \quad r_l \triangleq (2n+1)d_{\text{sat}},$$

Its arbitrary row-wise linear formation illustrated in Fig. 2c has the distance vector $R_l(\tau) \in \mathbb{R}^3$ from the $(-n)$ th satellite to the (n) th satellite as

$$R_l(\tau) \triangleq r_l(\tau) \hat{p}(\tau) \parallel p_d(\tau), \quad \tau \in [0, 2\pi/\omega_{xy}).$$



(a) Planar-array antenna. (b) Distributed space antenna [1], [29].

1-Layer Magnetorquer

$2r_{\text{coil}} [m]$

$2a_{\text{coil}} [m]$

$R = d_{\text{sat}} \times n [m]$

$d_{\text{sat}} [m]$

$2a_{\text{sat}} [m]$

S/C -1 S/C 0 S/C 1 S/C 2 S/C n

Group: ω_{f2} Group: ω_{f1} Group: ω_{f0} Group: ω_{f1} Group: ω_{f2} Group: ω_{fn-1}

(c) Linear formation model of $2n+1$ satellites [26].

Fig. 2. Grid-structured approximation for distributed space system design. This formation consists of equally spaced linear arrays.

Example 1. The distance d_{sat} is set to be no greater than half a wavelength λ to suppress grating lobes—undesired radiation with comparable strength to the main lobe peak.

$$d_{\text{sat}} \triangleq \text{const.} \leq \lambda/2. \quad (24)$$

Definition 2. The total system mass m_{sys} and its relaxed constraint are defined by the total number of satellites $N_{\text{all}} = (2n+1)^2$ by (23) in Assumption 1:

$$N_{\text{all}} m_{\text{sat}} \triangleq \bar{m}_{\text{sys}}, \quad |N_{\text{all}} m_{\text{sat}} - \bar{m}_{\text{sys}}| \leq \gamma_{\text{sys}}, \quad (25)$$

where \bar{m}_{sys} is the user-defined total system mass and γ_{sys} is the tolerance of the total system mass for computation.

2) *Decentralized Control Model*: To suppress unintended coupling among nonadjacent satellites in close proximity, we first assume the use of frequency allocation introduced in subsection II-D to confine electromagnetic interactions to neighboring satellites.

Assumption 2. Control pairs are defined by assigning distinct AC angular frequencies ω_{fk} for $k \in [-n, n]$ to adjacent satellite groups, as illustrated in Fig. 2c (Please refer the detailed selection of angular frequencies [20]).

IV. DISTRIBUTED ANTENNA DESIGN OPTIMIZATION

This section presents a nonconvex optimization-based framework to evaluate the feasibility of distributed space antennas. In practice, however, excessively increasing the number

of satellites would lead to unrealistically small satellites due to physical density limits. In the next section, considering these practical constraints, the detailed design problem is formulated as a nonconvex optimization problem, yielding feasible design solutions and more refined scaling trends.

A. Overview of Design Optimization Problem

We provide an overview of the design framework for the distributed space antenna and clarify the constraints. We consider the design parameters X of our framework for a given satellite distance d_{sat} in (24) of Example 1 and system mass \bar{m}_{sys} in Assumption 1:

$$X = \{2a_{\text{coil}}, 2a_{\text{sat}}, q_{\text{coil}}, n, u_{\text{msl}}\}, \quad (26)$$

where the coil diameter $2a_{\text{coil}}$, satellite size $2a_{\text{sat}}$, coil parameter q_{coil} , satellite number n , and peak sidelobe variable u_{psl} . Then, the design optimization \mathcal{P}_{DSA} is formulated as follow:

$$\begin{aligned} X^* = \arg \min_{X \in \mathcal{X}_{\text{feas}}} L_{\text{bw}} = \arg \max_{X \in \mathcal{X}_{\text{feas}}} N_{\text{all}} \quad \text{subject to:} \\ \left\{ \begin{array}{l} \text{(A) Satellite specification constraints} \\ \text{(B) Phased-array antenna constraints} \\ \text{(C) Magnetic formation-keeping constraints} \end{array} \right. \quad (27) \end{aligned}$$

where the constraints in (A)–(C) are described in Subsections IV-B, IV-C, and IV-D, respectively. The optimal X^* yields other dependent parameters, such as the generation and consumption power, EIRP, and component masses.

B. Constraints 1/3: Satellite Specification

This section defines the design parameters for each satellite and formulates the power consumption and satellite constraints. We define the satellite configuration as follows.

Definition 3. *The satellite consists of 1) an identical three-axis coil, 2) solar panels, 3) a battery, 4) a satellite body, and 5) a bus that includes antennas, transmitters, and avionics:*

$$m_{\text{sat}} \triangleq m_{3\text{coil}} + m_{4\text{sap}} + m_{\text{bat}} + m_{\text{str}} + m_{\text{bus}},$$

where each term corresponds to the mass of each subsystem.

1) *Component Size Constraints:* This subsection summarizes the constraints on the satellite and coil sizes. Size is a critical parameter that involves trade-offs between mass, power acquisition, and achieving of the magnetic moment. We formulate Assumption 3 considering the obvious physical constraints of satellites.

Assumption 3. *The geometric relationship among the satellite radius, coil radius, and inter-satellite distance is illustrated in Fig. 2c. The coil radius a_{coil} is smaller than the satellite one a_{sat} and $2a_{\text{sat}}$ is smaller than the distance between the satellite centers d_{sat} with the coil size margin r_{mar}*

$$a_{\text{coil}} \stackrel{\Delta}{\leq} a_{\text{sat}} - r_{\text{mar}}, \quad 2a_{\text{sat}} \stackrel{\Delta}{\leq} d_{\text{sat}}, \quad k_F a_{\text{coil}} \stackrel{\Delta}{\leq} d_{\text{sat}}, \quad (28)$$

where the final inequality is from the assumption that the distance between the coils is sufficiently large compared with the coil radius with defined coefficient k_F .

2) *Component Mass Definitions and Assumptions:* This subsection defines the masses of the satellite components. We implement Assumption 4 based on Definition 3 to define the component masses $m_{3\text{coil}}$, $m_{4\text{sap}}$, m_{bat} , m_{str} , and m_{bus} as dependent parameters of the other parameters.

Assumption 4. *The satellite has a cubic shape and an identical three-axis coil, that is, with an equal number of turns N_t , wire radius r_{coil} , and coil radius a_{coil} . Solar panels are attached to the four sides of the satellite. The bus mass m_{bus} is treated as a user-defined constant, $m_{\text{bus}0}$. The structural mass m_{str} is defined as a proportion of the total satellite mass. P_{sap} denotes the power generated during sunlit operation:*

$$P_{\text{sap}}(a_{\text{sat}}) \triangleq k_{\text{sap}} P_{\text{W/m}^2} (2a_{\text{sat}})^2, \quad (29)$$

where $P_{\text{W/m}^2}$ is the power generated per unit area of the solar panel and k_{sap} is the effective area coefficient.

The battery storage requirement is modeled as the solar energy that is harvested over a sunlit charging duration h_{charge} and a design coefficient that captures the charging efficiency and usable fraction k_{bat} using P_{sap} in (29).

Example 2 (Requirement for battery storage from sunlit charging). *As a concrete sizing example, consider a baseline case in which the satellite stores 10% of the energy that is harvested during a 12-h sunlit period. This corresponds to setting $k_{\text{bat}} = 0.1$ and $h_{\text{charge}} = 12$. Under this setting, the required battery storage is modeled as*

$$k_{\text{bat}} h_{\text{charge}} P_{\text{sap}}(a_{\text{sat}}) = 1.2 P_{\text{sap}}(a_{\text{sat}}), \quad (30)$$

where $P_{\text{sap}}(a_{\text{sat}})$ is determined by (29).

This Assumption 4 defines the mass of the three-axis coil with the coil parameter q_{coil} , four solar panels, battery, structure, and bus system:

$$\left\{ \begin{array}{l} m_{3\text{coil}}(a_{\text{coil}}, q_{\text{coil}}) \triangleq 3(2\pi^2 a_{\text{coil}}) q_{\text{coil}} \rho_c, \\ q_{\text{coil}} \triangleq N_t r_{\text{coil}}^2, \\ m_{\text{sap}}(a_{\text{sat}}) \triangleq \nu_{\text{sap}} \rho_{\text{sap}} (2a_{\text{sat}})^2, \\ m_{\text{bat}}(a_{\text{sat}}) \triangleq \rho_{\text{bat}} k_{\text{bat}} h_{\text{charge}} P_{\text{sap}}(a_{\text{sat}}), \\ m_{\text{str}}(m_{\text{sat}}) \triangleq \eta_{\text{str}} m_{\text{sat}}, \\ m_{\text{bus}} \triangleq m_{\text{bus}0} = \text{const}, \end{array} \right. \quad (31)$$

where ρ_c denotes the mass density of the wire, ρ_{sap} is the mass per unit area density, ν_{sap} is the number of solar panels that are mounted on the satellite, η_{str} is a user-defined constant, and ρ_{bat} is the mass per unit power capacity of the battery. Throughout this study, P_{bat} is modeled as a function of the satellite volume. The coil parameter q_{coil} in (31) allows N_t and r_{coil} to be adjusted according to the satellite geometry by obtaining the optimal q_{coil} .

3) *Component Mass Constraints:* Finally, we calculate the component mass constraints. As indicated in (31), our assumption limits the masses of almost all components as dependent variables of a_{sat} , except for the coil mass $m_{3\text{coil}}(a_{\text{coil}}, q_{\text{coil}})$. This $m_{3\text{coil}}$ should be designed to satisfy the requirements of antenna performance and formation control. Subsequently, we derive the upper bound \bar{m}_{sat} to avoid impractical coil configurations by assuming that $m_{\text{sat}} \propto a_{\text{sat}}^3$. Because the

TABLE I
PREVIOUS SATELLITE DESIGNS

	V (cm ³)	m_{sat} (g)
[15]	$2 \times 2 \times 0.075$	10
[33]	$9 \times 9.5 \times 1$	70
[34]	$9 \times 9 \times 1$	100
[12]	$4 \times 4 \times 4.25$	95.5
[35], [36]	$3.3 \times 3.3 \times 0.5$	9.9

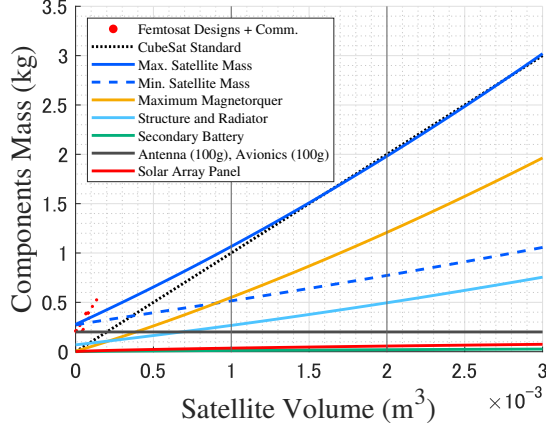


Fig. 3. Relationship between satellite volume and component mass.

total mass should converge to a finite lower bound, we statistically derive this relationship from the existing satellite design parameters.

Assumption 5. \bar{m}_{sat} is a polynomial function of a_{sat} :

$$\bar{m}_{\text{sat}}(a_{\text{sat}}) \triangleq \begin{cases} k_{\bar{m}} a_{\text{sat}}^3 & \text{if } 2a_{\text{sat}} \geq 0.1 \\ f_{\text{emp}}(a_{\text{sat}}) & \text{otherwise,} \end{cases} \quad (32)$$

where $k_{\bar{m}}$ is an arbitrary parameter for which we mainly select $k_{\bar{m}} = 1e^3$ for the standard CubeSat design, and $f_{\text{emp}}(a_{\text{sat}})$ denotes an empirically approximated function that is obtained by fitting the previously designed satellite mass, e.g., the parameters in Table I and red markers in Fig. 3.

This methodology using f_{emp} yields design solutions that are consistent with current technology and is adaptable using updated data from next-generation satellites. Subsequently, we derive the upper and lower bounds $m_{\text{sat}}(a_{\text{sat}})$ and

$$m_{\text{sat}} \triangleq \bar{m}_{\text{sat}}(a_{\text{sat}}) \quad (33)$$

$$m_{4\text{sap}}(a_{\text{sat}}) + m_{\text{bat}}(a_{\text{sat}}) + m_{\text{str}}(m_{\text{sat}}) + m_{\text{bus}} \triangleq m_{\text{sat}},$$

where $\bar{m}_{\text{sat}}(a_{\text{sat}})$ is determined by (32) and the lower bound is derived as $m_{3\text{coil}} = 0$.

C. Constraints 2/3: Phased-Array Antenna

The antenna performance constraints of the distributed space antenna are formulated in this section. We adopt a simplified antenna model consisting of an $N_l \times N_l$ square grid to render the analysis tractable while preserving system-level trends.

1) *Tractable Beam Footprint Model:* We first formulate a computationally tractable beam footprint model by approximating the beam edge with the first null of the main lobe. The footprint boundary is characterized by the beamwidth in the diagonal cut ($\phi = \pi/4$), which reduces the two-dimensional beam projection to a uniaxial representation.

Assumption 6 (Azimuth restriction for footprint evaluation). *The azimuth is fixed at $\phi = \phi_0 = \pi/4$, that is, the diagonal cut where $u_x = u_y = u$, to reduce the dimensionality of the footprint evaluation.*

Under this restriction, the two-dimensional normalized field array factor of the square grid array is transformed into

$$A_{\text{diag}}(u) = \left(\frac{\sin(N_l u)}{N_l \sin(u)} \right)^2, \quad u = \frac{k d_{\text{sat}}}{\sqrt{2}} (\sin \theta - \sin \theta_0). \quad (34)$$

Here, $A_{\text{diag}}(u)$ is the direction-restricted normalized field array factor. The corresponding normalized gain pattern is given by $|A_{\text{diag}}(u)|^2$, but only the null location of $A_{\text{diag}}(u)$ is required for the footprint approximation. The beam edge is therefore defined by the first null condition $N_l u = \pi$, which yields the null angle θ_{n1} .

Assumption 7 (Footprint Definition). *The beam footprint is defined by the first null of the main lobe evaluated along the specific azimuth direction defined in Assumption 6. It is assumed that the orbital altitude h is significantly larger than the element spacing d_{sat} , i.e., $h \gg d_{\text{sat}}$.*

Using the geometric relationship based on Assumption 7, the footprint diameter D_{fp} is derived as a function of θ_{n1} and the orbital altitude h :

$$\theta_{n1} \triangleq \arcsin \left(\frac{\sqrt{2}\lambda}{N_l d_{\text{sat}}} + \sin \theta_0 \right), \quad D_{fp} \approx 2|\theta_{n1} - \theta_0|h. \quad (35)$$

2) *Peak-Sidelobe and Transmitter Power Derivation:* The local maximizer of $B_{\text{env}}(u)$ within the first sidelobe region defines the peak-sidelobe envelope point u_{psl} :

$$\begin{cases} N_l \sin(u_{\text{psl}}) \cos(N_l u_{\text{psl}}) - \cos(u_{\text{psl}}) \sin(N_l u_{\text{psl}}) \triangleq 0, \\ \frac{\pi}{N_l} \triangleq |u_{\text{psl}}| \triangleq \frac{2\pi}{N_l}. \end{cases} \quad (36)$$

For peak-sidelobe-constrained transmit-power sizing, we use the one-dimensional sidelobe envelope of the separable square array. From the separable field array factor in (19) and the normalized gain definition in (18), the two-dimensional response can be expressed as

$$B_{2D}(u_x, u_y) = B_x(u_x) B_y(u_y),$$

where B_x and B_y are normalized by the main-beam peak. Since the maximum contribution from the other array axis is unity, i.e., $\max_{u_y} B_y(u_y) = 1$, the largest two-dimensional response for a given $u_x = u$ is bounded by

$$\max_{u_y} B_{2D}(u, u_y) = B_x(u) \max_{u_y} B_y(u_y) = B_x(u).$$

Therefore, the sidelobe-envelope measure used in this study is defined as

$$B_{\text{env}}(u) = B_x(u) = \left| \frac{\sin(N_l u)}{N_l \sin(u)} \right|^2. \quad (37)$$

This quantity is a dimensionless normalized gain pattern used for system-level sizing. It is distinguished from the direction-restricted field array factor $A_{\text{diag}}(u)$ used for the footprint approximation. The sidelobe EIRP evaluated by the envelope model must be smaller than the received power indicator I_R :

$$\text{EIRP}_{\text{max}} B_{\text{env}}(u_{\text{psl}}) \stackrel{\Delta}{\leq} I_R. \quad (38)$$

The RF transmit power satisfying the equality in (38) is obtained from $\text{EIRP}_{\text{max}} = P_t N_l^4$ and (37) as follows:

$$P_t \triangleq \frac{I_R}{N_l^4 B_{\text{env}}(u_{\text{psl}})} = \frac{I_R}{N_l^2} \left(\frac{\sin(u_{\text{psl}})}{\sin(N_l u_{\text{psl}})} \right)^2. \quad (39)$$

Remark 1. Assuming a direct-to-device (D2D) communication scenario, I_R is expressed as an example as follows:

$$I_R \triangleq \zeta P_R L_f / G_R, \quad L_f = \left(\frac{4\pi h}{\lambda} \right)^2, \quad (40)$$

where P_R is the required received power, G_R is the antenna gain, $\zeta \in (0, 1]$ is the attenuation factor, and L_f is the free-space path loss. Then, the transmit power is

$$P_t \triangleq \frac{\zeta P_R L_f}{N_l^2 G_R} \left(\frac{\sin(u_{\text{psl}})}{\sin(N_l u_{\text{psl}})} \right)^2. \quad (41)$$

Remark 2. The variable u_{psl} is introduced to specify the finite-array peak point of the sidelobe envelope used in transmit-power sizing. It is not intended to represent a full two-dimensional radiation-pattern search.

D. Constraints 3/3: Magnetic Formation-Keeping

We describe the power requirements for a distributed space antenna to execute its communication mission while maintaining relative inter-satellite positions against disturbances.

1) *Power Budget for Steady-Formation Maintenance:* A steady-state power-budget constraint for long-term magnetic formation maintenance is formulated in this subsection.

Definition 4. The steady-state power consumption includes a control power P_{cont} , mission power P_{mis} , bus power P_{bus} , and margin power P_{mar} , where P_{bus} is a constant:

$$P_{\text{tot}} \triangleq P_{\text{cont}} + P_{\text{mis}} + P_{\text{bus}} + P_{\text{mar}}. \quad (42)$$

Assumption 8. As a steady-state condition, the power is supplied only by solar panels, and the time-averaged consumption remains below the generated power: $P_{\text{tot}} \leq P_{\text{sap}}$.

Assumption 9. The required power for each axis is evaluated from the peak coil output. The control power for one axis is defined as

$$P_{\text{1axis}} = R_{\text{coil}} c_{\text{coil}}^2 = \frac{2p_c \bar{\mu}_{2\text{dir}}^2}{\pi^2 q_{\text{coil}} a_{\text{coil}}^3}, \quad (43)$$

where R_{coil} is the coil resistance defined in (10), c_{coil} is the coil current, and $\bar{\mu}_{2\text{dir}}$ is the upper bound of magnetic moment required for bidirectional compensation along one axis.

When AC actuation is used to alternate the moment command between two opposite directions along one axis, the synthesized magnetic moment $\mu_{2\text{dir}}(t)$ is written as

$$\begin{aligned} \mu_{2\text{dir}}(t) &= \mu_{1\text{dir}} \cos(\omega_{f_n} t) + \mu_{1\text{dir}} \cos\left(\omega_{f_n} t + \frac{\pi}{2}\right) \\ &= \sqrt{2} \mu_{1\text{dir}} \sin\left(\omega_{f_n} t + \frac{\pi}{4}\right), \end{aligned} \quad (44)$$

where ω_{f_n} is the AC frequency assigned to the n -th satellite and the upper bound of $\bar{\mu}_{2\text{dir}}$ is $\sqrt{2} \mu_{1\text{dir}}$. Accordingly, the total control power at the central satellite is given by

$$P_{\text{cont}} = P_{2\text{axis}} = 2P_{\text{1axis}}. \quad (45)$$

We also model the mission power P_{mis} as the transmitter power consumption and the margin power P_{mar} for another purpose, e.g., deployment, are defined as

$$P_{\text{mis}} = P_t / \eta_{\text{tra}}, \quad P_{\text{mar}} = \frac{2p_c \bar{\mu}_{\text{mar}}^2}{\pi^2 q_{\text{coil}} a_{\text{coil}}^3}, \quad (46)$$

where η_{tra} is the transmitter efficiency and P_t is the per-satellite transmit power and $\bar{\mu}_{\text{mar}}$ denotes the upper bound of margin magnetic moment.

2) *Magnetic Moment Estimation by Numerical Integration:* We numerically calculate the power consumption during steady-state operations for a square-grid formation. We compute the maximum control power at each time step through actual numerical simulations in order to evaluate the largest power consumption within the formation. This avoids the conservatism of the convex optimization-based power analysis in [26], which assumes perfect disturbance cancellation. Although the optimal values J_d^* in (16) are equal to the total squared magnetic-dipole requirement over the three axes [26], the problem in (16) does not specify its axis-wise allocation. Then, we adopt the simplified coil-sizing assumption.

Assumption 10. A single-axis coil is sized to meet the worst-case axis power demand, and the same coil specification is applied to all three axes. By removing the time-averaging factor and considering the peak requirement, the one-direction magnetic moment μ_{1d} is defined as

$$\mu_{1d}^2 \triangleq J_d^*(n). \quad (47)$$

Instead of strictly stabilizing the formation to an exact target trajectory, we relax the control objective. As an example, this study considers stabilizing the satellites within a tolerable position-error bound sufficient for antenna functionality to improve performance. The drift term in (5) increases the relative distance between satellites over time and negatively affects the connectivity maintenance. Then, we apply previous controller [1], [29] to reduce both the drift and the control input. Its closed-loop system related to this drift term [1], [29]:

$$\begin{bmatrix} \dot{e}_{-2C_1} \\ \dot{e}_{C_4} \end{bmatrix} = \begin{bmatrix} -\frac{k_A}{2} L_e & O \\ \frac{\epsilon_2}{2} \left(I - \frac{\gamma k_\gamma}{2} L_e \right) & -\frac{\gamma k_A}{2} L_e \end{bmatrix} \begin{bmatrix} e_{-2C_1} \\ e_{C_4} \end{bmatrix} - k_0 \begin{bmatrix} e_{d_y} \\ e_{d_x} \end{bmatrix} \quad (48)$$

where $e_{-2C_1} = E^\top[-2C_1]$, $e_{C_4} = E^\top[C_4]$, and $e_{d_{x,y}} = E^\top[d_{x,y}]$. We construct approximate function $J_d^*(n)$ by exhaustively solving (16) for each n in Section V-A. We emphasize that we can replace with different controllers and control objectives.

Remark 3. *Our goal is to evaluate the steady states of the formation keeping for $N_{\text{all}} \gg 1$ using scalable computational methods. Since the theoretical bound estimation of the steady state can yield conservative results for $N_{\text{all}} \gg 1$ [2], we utilize the numerical estimation to derive its exact values. One drawback to using the numerical method is the high computational costs as the number of satellites grows. For example, we consider the linear time-invariant system $\dot{x} = Ax(t) + d(t)$. The previous study [26] avoids conducting a straightforward numerical integration, such as the fourth-order Runge–Kutta method, and deriving analytical solutions for its analytical solution under $x(0) = 0$:*

$$x(T) = \int_0^T e^{A(T-\tau)} d(\tau) d\tau = \sum_{k=1}^K \left[\int_{t_k}^{t_{k+1}} e^{A(T-\tau)} d\tau \right] d_k,$$

where $d(t) = d_k$ for $t \in [t_k, t_{k+1})$, $A \in \mathbb{R}^{N_{\text{all}} \times N_{\text{all}}}$ is a stable matrix, and $d(t) \in \mathbb{R}^{N_{\text{all}}}$ is a time-varying external input. Previous study [26] shows its computational costs can be reduced to $\mathcal{O}(4N_{\text{all}}^2 K)$ or $\mathcal{O}(N_{\text{all}}^3) + \mathcal{O}(N_{\text{all}}^2 K/P)$ with the parallelism P , which takes a high computational cost. In Section V-A, we use Krylov subspace methods [37] to reduce the total costs for $N_{\text{all}} \gg 1$. This method approximately derives $e^{A(T-\tau_j)} d(\tau_j)$ with a cost of $\mathcal{O}(N_{\text{all}} \log N_{\text{all}})$ and the final cost is $\mathcal{O}(N_{\text{all}} \log N_{\text{all}} K/P)$, making the computation more tractable than direct numerical integration.

E. Overall Framework and Feasibility Region

We integrate the objectives and constraints introduced in previous sections into a optimization-based design framework \mathcal{P}_{DSA} in (27) and the overall procedure is summarized in Algorithm 1 with user-defined evaluation function $\mathcal{J}(X)$ and the constraints in (A)–(C) are described in Subsections IV-B, IV-C, and IV-D, respectively.

To avoid an infeasible start of our nonconvex optimization problem, this subsection also denotes a warm-start strategy to specify the feasibility region χ_{feas} of design parameters $X = \{2a_{\text{coil}}, 2a_{\text{sat}}, q_{\text{coil}}, n, u_{\text{msl}}\}$ in (26). Here, (\cdot) and $(\bar{\cdot})$ denote the lower and upper bounds, subscript 0 denotes the initial value, and $\xi_i \sim \mathcal{U}(0, 1)$ are independent samples. The primary geometric variables are drawn uniformly within their bounds and then capped by simple geometric limits:

$$\begin{aligned} a_{\text{coil}0} &= \min\left(\frac{d_{\text{sat}}}{k_F}, \underline{a}_{\text{coil}} + \xi_2(\bar{a}_{\text{coil}} - \underline{a}_{\text{coil}})\right), \\ a_{\text{sat}0} &= \min\left(\frac{d_{\text{sat}}}{2}, \underline{a}_{\text{sat}} + \xi_1(\bar{a}_{\text{sat}} - \underline{a}_{\text{sat}})\right), \\ m_{\text{sys}0} &= \underline{m}_{\text{sys}} + \xi_3(\bar{m}_{\text{sys}} - \underline{m}_{\text{sys}}). \end{aligned} \quad (49)$$

Then, we compute the remaining mass budget for the coil wiring, denoted $\bar{m}_{\text{coil}0}$, and translate it into \bar{q}_{coil} using the

Algorithm 1 Distributed space antenna design framework

- 1: **Input:** 1) satellite distance d_{sat} , system mass \bar{m}_{sys} , and investigation parameters χ_{inv} : {e.g., margin magnetic moment $\bar{\mu}_{\text{mar}}$ or transmit power P_t } 2) feasible region χ_{feas} for design parameters {coil diameter $2a_{\text{coil}}$, satellite size $2a_{\text{sat}}$, coil parameter q_{coil} , satellite number n , and maximum sidelobe variable u_{psl} } in Table II, 3) multi-start trials N_{GS} , 4) constants in Table II, 5) user-defined evaluation function $\mathcal{J}(X)$
- 2: **Output:** Optimal X^* and other parameters $f(X^*)$: generation and consumption power, EIRP, satellite and component masses $m_{\text{sat}} = m_{3\text{coil}} + m_{4\text{sap}} + m_{\text{bat}} + m_{\text{str}} + m_{\text{bus}}$
- 3: **for** $s = 1, \dots, N_{\text{GS}}$ **do**
- 4: Generate random $X_0^{(s)} \in \chi_{\text{feas}}$ and solve \mathcal{P}_{DSA}
- 5: **end for**
- 6: Select the best solution X^* that maximizes $\mathcal{J}(X)$
- 7: _____
- 8: Distributed array design optimization $\mathcal{P}_{\text{DSA}}(d_{\text{sat}}, m_{\text{sys}})$

$$X^* = \arg \max_{X \in \chi_{\text{feas}}} \mathcal{J}(X) \quad \text{subject to:}$$

- (A) Satellite specification constraints
 - $a_{\text{coil}} \leq a_{\text{sat}} - r_{\text{mar}}, \quad k_F a_{\text{coil}} \leq d_{\text{sat}}$
 - $2a_{\text{sat}} \leq d_{\text{sat}}, \quad \left| \frac{m_{\text{sys}}}{N_{\text{all}}} - m_{\text{sat}} \right| \leq \gamma_{\text{mass}}$
 - $\bar{m}_{\text{sat}}(a_{\text{sat}}) - m_{3\text{coil}} - m_{4\text{sap}} \leq m_{\text{sat}} \leq \bar{m}_{\text{sat}}(a_{\text{sat}})$
 - $|\bar{m}_{\text{sys}} - m_{\text{sys}}| \leq \gamma_{\text{sys}}$
 - $P_{\text{cont}} + P_{\text{mis}} + P_{\text{bus}} + P_{\text{mar}} \leq P_{\text{sap}}$
- (B) Phased-array antenna constraints
 - $|N_l \sin(u_{\text{psl}}) \cos(N_l u_{\text{psl}}) - \cos(u_{\text{psl}}) \sin(N_l u_{\text{psl}})| \leq \gamma_{\text{psl}}$
 - $\frac{\pi}{N_l} < |u_{\text{psl}}| < \frac{2\pi}{N_l}, \quad P_{\text{mis}} = P_t / \eta_{\text{tra}}$
 - $G_T = \bar{D} \approx N_l^2, \quad P_t \triangleq \frac{I_R}{N_l^2} \left(\frac{\sin(u_{\text{psl}})}{\sin(N_l u_{\text{psl}})} \right)^2$
- (C) Magnetic formation-keeping constraints
 - $4P_{1\text{d-cont}} = 4 \frac{2p_c \mu_{1\text{d-cont}}^2}{\pi^2 q_{\text{coil}} a_{\text{coil}}^3}, \quad \mu_{1\text{d-cont}}^2 = J_d^*(n)$

coil-mass model (Definition 3 and Assumption 4):

$$\begin{aligned} q_{\text{coil}} &\leq \bar{q}_{\text{coil}0} \triangleq \bar{m}_{\text{coil}0} / (6\pi^2 \rho_c a_{\text{coil}0}), \\ q_{\text{coil}0} &= \underline{q}_{\text{coil}} + \xi_6 \left(\min(\bar{q}_{\text{coil}0}, \bar{q}_{\text{coil}}) - \underline{q}_{\text{coil}} \right). \end{aligned} \quad (50)$$

Note that we bound q_{coil} in (31)

$$q_{\text{coil}} \in [\underline{N}_t r_{\text{coil}}^2, \bar{N}_t \bar{r}_{\text{coil}}^2] \quad (51)$$

where the \underline{N}_t and \bar{N}_t define

$$\left\{ \underline{N}_t = 1, \quad \bar{N}_t = \frac{\bar{a}_{\text{sat}}}{L_{\text{coil}}} \right. \quad (52)$$

Next, n is sampled using an instance-dependent upper bound obtained from the empirical mass model in Assumption 5.

We enforce $m_{\text{sys}0}/(2n_0 + 1)^2 \geq \underline{m}_{\text{sat}}$ and solving this for n_0 yields

$$n_0 \leq \bar{n} \triangleq \left(-1 + \sqrt{m_{\text{sys}0}/\underline{m}_{\text{sat}}}\right)/2, \quad (53)$$

to avoid unrealistically small satellite masses, and we use

$$n_0 = \underline{n} + \xi_4 (\bar{n} - \underline{n}). \quad (54)$$

The initial value $u_{\text{psl}0}$ is randomly generated within a narrowed subset of its theoretical peak-sidelobe neighborhood. By introducing a small positive tolerance γ_u to the interval boundaries, the warm-start point is determined as follows:

$$u_{\text{psl}0} = \left(\frac{(1 - 2\gamma_u)\pi}{2n_0 + 1}\right) \xi_5 - \frac{(2 - \gamma_u)\pi}{2n_0 + 1}. \quad (55)$$

This formulation ensures that $u_{\text{psl}0}$ is constrained within the range $\left[\frac{(-2 + \gamma_u)\pi}{2n_0 + 1}, \frac{(-1 - \gamma_u)\pi}{2n_0 + 1}\right]$, providing a well-conditioned starting point for the subsequent local optimization.

V. ARRAY DESIGN EXAMPLES AND DISCUSSION

This section presents design examples obtained through the proposed framework and highlights the design trends of EMFF-based distributed space antennas.

A. Analysis of Representative Case Studies

To demonstrate the applicability of the proposed framework, this subsection considers three design scenarios. For Case 1, the design objective is to achieve a narrow beam by minimizing the footprint. This objective can be written as

$$\arg \min_{\mathcal{X}} \arcsin \left(\frac{\sqrt{2}\lambda}{N_l d_{\text{sat}}} + \sin \theta_0 \right) = \arg \max_{\mathcal{X}} N_{\text{all}}. \quad (56)$$

For Cases 2 and 3, the design objective is to maximize the communication or sensing capability. In these cases, the EIRP maximization problem is likewise reduced to the maximization of N_{all} :

$$\arg \max_{\mathcal{X}} \text{EIRP} \propto \arg \max_{\mathcal{X}} (P_t N_l^2 \cdot G_T) = \arg \max_{\mathcal{X}} N_{\text{all}}. \quad (57)$$

The numerical settings are shared across the three case studies to ensure a consistent comparison. All design solutions are obtained using Algorithm 1 and MATLAB's GlobalSearch solver [41]. The constants and feasible design ranges are listed in Table II, and the overall system mass is varied from 500 kg to 6000 kg. The disturbance-compensation requirement enters the EMFF power model through $J_d^*(n)$: according to (47), $J_d^*(n)$ determines the required single-axis magnetic moment, and this value is then used in the control-power expressions in (46). Therefore, $J_d^*(n)$ is estimated in advance as a function of the satellite number for each inter-satellite distance. We numerically integrate (48) for a square-grid formation with fixed spacing d_{sat} m over multiple values of k_A . Based on Fig. 4, we select $k_A = 0.0560$. For this k_A , we derive J_d as a function of the number of satellites from the relationship between the position error and the control input. Figure 4 shows the fitted $J_d^*(n)$ curves for $d_{\text{sat}} = 0.15$ m and $d_{\text{sat}} = 0.60$ m, and these fitted curves are used in the EMFF power constraint during the optimization.

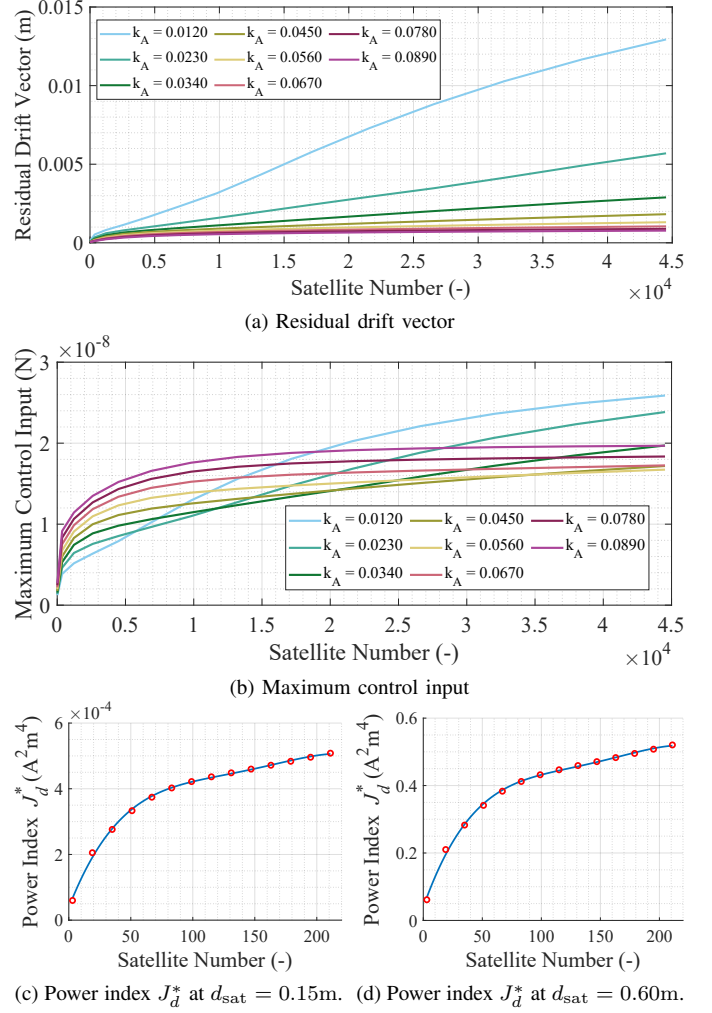


Fig. 4. Numerical estimation of the distributed-control requirement used in the EMFF power constraint. Panels (a) and (b) show the residual drift vector and maximum control input obtained from the distributed formation-control simulation for different feedback gains k_A . Based on these results, $k_A = 0.0560$ is selected as the nominal gain used to construct the control requirement. Panels (c) and (d) show the resulting power index $J_d^*(n)$ for $d_{\text{sat}} = 0.15$ m and $d_{\text{sat}} = 0.60$ m, respectively. The red circles denote the numerical values obtained by solving the magnetic-dipole allocation problem in (16), and the blue curves denote the fourth-order polynomial fits used in the design optimization.

1) *Case 1: Margin Magnetic Moment Analysis:* Case 1 evaluates how the margin magnetic moment affects footprint-oriented antenna sizing in a D2D-oriented 1-GHz case with $\lambda = 0.30$ m and $d_{\text{sat}} = 0.15$ m. This spacing corresponds to half a wavelength. The per-element RF transmit power P_t is calculated from the peak-sidelobe-envelope-limited model in (41) using the D2D received-power requirement, and $\bar{\mu}_{\text{mar}}$ is treated as the investigation parameter representing the control capability reserved beyond disturbance compensation. The numerical setup, representative design values, optimized trends, and constraint margins are shown in Table III, Table IV, Fig. 5, and Figs. 8a–8c, respectively.

2) *Case 2: Transmit-Power Analysis:* Case 2 evaluates how prescribed transmit power affects EIRP and satellite sizing at $\lambda = 0.30$ m and $d_{\text{sat}} = 0.15$ m. The margin magnetic moment is fixed at $\bar{\mu}_{\text{mar}} = 0.25$ Am², and P_t is treated as the inves-

TABLE II

CALCULATION CONSTANTS OF DESIGN PARAMETERS FOR ALGORITHM 1: DISTRIBUTED SPACE ANTENNAS DESIGN.		
Satellite Design Parameters		Orbital and Communication Constants
Description	Constant	Value
Resistivity of wire	p_c (10)	$1.68e^{-8}\Omega\text{m}$ [38]
Mass density of wire	ρ_c (31)	8960 kg/m^3 [39]
Mass per unit power capacity of the battery	ρ_{bat} (31)	0.005 kg/Wh
Mass per unit area of the solar panel	ρ_{sap} (31)	0.6 kg/m^2
Number of solar panels	ν_{sap} (31)	4
Power generation per unit area of solar panel	$P_{\text{W/m}^2}$ (29)	$1367 \times 0.3\text{ W/m}^2$
Effective area coefficient	k_{sap} (29)	1
Coefficient of structure mass	η_{str} (31)	0.25
Margin of coil size	r_{mar} (28)	0.005 m
Bus power	P_{bus} (42)	0.200 W
Bus mass	m_{bus} (31)	0.200 kg
Battery storage coefficient	k_{bat} (30)	0.1
Satellite/system-mass tolerance	$\gamma_{\text{mass}}/\gamma_{\text{sys}}$	$10^{-2}/10^{-2}$
Peak-sidelobe/ $u_{\text{psl}0}$ tolerance	$\gamma_{\text{psl}}/\gamma_{\text{u}}$	$10^{-5}/0.1$

Feasible region χ_{feas} of optimization variable		
Variable	Min	Max
System mass m_{sys}	$(1 - \gamma_{\text{sys}})\bar{m}_{\text{sys}}$	$(1 + \gamma_{\text{sys}})\bar{m}_{\text{sys}}$
Satellite radius a_{sat}	0.015	$d_{\text{sat}}/2$
Coil radius a_{coil}	0.005	$d_{\text{sat}}/2 - r_{\text{mar}}$
Coil parameter q_{coil}	$N_t r_{\text{coil}}^2$	$N_t \bar{r}_{\text{coil}}^2$
Satellite number n	3	\bar{n}
Peak sidelobe variable u_{psl}	$-2\pi/3$	0

Note: The lower and upper bounds of the coil-wire radius used in the bounds of q_{coil} are $r_{\text{coil}} = 0.03937 \times 10^{-3}$ m and $\bar{r}_{\text{coil}} = 0.00105$ m, respectively.

tigation parameter; unlike Case 1, the peak sidelobe level is evaluated as an output rather than used to determine P_t inside the optimization. The numerical setup, representative design values, optimized trends, and constraint margins are shown in Table V, Table VI, Fig. 6, and Figs. 8d–8f, respectively.

3) *Case 3: Large-Spacing Feasibility Analysis:* Case 3 evaluates the feasibility limit caused by increasing the inter-satellite spacing to $d_{\text{sat}} = 0.60$ m with $\lambda = 1.20$ m. The margin magnetic moment is fixed at $\bar{\mu}_{\text{mar}} = 0.25\text{ Am}^2$, and P_t is swept as in Case 2 to compare how the larger spacing increases the coil burden required for EMFF formation maintenance. The numerical setup, representative design values, optimized trends, and constraint margins are shown in Table VII, Table VIII, Fig. 7, and Figs. 8g–8i, respectively.

B. Discussion

1) *System-Level Trade-Off:* The three case studies show that aperture enlargement improves antenna performance only while the satellite-level design retains sufficient headroom for EMFF control. Figure 5 and Fig. 6 show that increasing the overall system mass generally enlarges the optimized aperture in the baseline-spacing cases, leading to footprint reduction in Case 1 and EIRP improvement in Case 2. Figure 7, however, shows that the large-spacing case reaches infeasible design points even when the overall system mass is increased. Figure 8 supports this interpretation by showing that, in Case 3, the satellite-size and power margins are already nearly exhausted while the satellite-mass margin decreases toward the upper-bound limit. Tables IV, VI, and VIII summarize the corresponding representative satellite specifications and antenna-performance values. The following subsections discuss the mechanisms that determine this design headroom: fixed-transmit-power simplification, margin magnetic moment, transmit power, and large inter-satellite spacing.

2) *Trends in Optimized Design Solutions:* Case 1 shows that requiring margin magnetic moment shifts the dominant design adjustment from coil diameter to coil parameter. For $d_{\text{sat}} = 0.15$ m, the coil diameter is limited by the distance-dependent coil-size constraint, as shown in Fig. 5h. Because P_{cont} and P_{mar} scale as $1/(q_{\text{coil}}a_{\text{coil}}^3)$, larger values of a_{coil}

reduce the required power and are therefore selected when allowed by the constraints; after this limit is reached, the remaining adjustment is made through q_{coil} , as shown in Fig. 5i. This increases the coil mass in Fig. 5f and reduces the power and size margins in Figs. 8c and 8b.

Case 2 should be interpreted as a sweep of non-coil mission power rather than as a general sensitivity analysis of transmit power. In this case, P_t is prescribed and increases the mission-power term, but it does not directly change the margin magnetic moment or the EMFF control requirement. Because this power increase is not large enough to substantially change the active satellite-level constraints, the optimized aperture and coil design remain nearly unchanged. Increasing P_t therefore mainly improves EIRP, as shown in Fig. 6c, while the antenna diameter changes only moderately in Fig. 6b. The design response appears mainly as satellite-size adjustment for additional power generation and the corresponding reduction in satellite-size margin, as shown in Figs. 6g and 8e.

Case 3 shows that the feasibility limit is governed by the coil burden required for large-spacing EMFF control. Figure 4 shows that $J_d^*(n)$ increases more severely for $d_{\text{sat}} = 0.60$ m than for $d_{\text{sat}} = 0.15$ m, while Figs. 8h and 8i show that the satellite-size and power margins are nearly exhausted. Since the coil diameter is limited by the satellite-size geometry in Fig. 7h, the optimizer increases q_{coil} instead, which increases the coil mass and drives the satellite mass toward its upper bound, as shown in Figs. 7i, 7f, and 8g. The comparison between Figs. 6c and 7c also shows that the coil mass fraction becomes larger in Case 3 than in Case 2, indicating that a larger portion of each satellite must be allocated to EMFF actuation under the large-spacing condition. Thus, the infeasible points arise from satellite-level mass, size, and power limits rather than from insufficient communication performance.

3) *Convex Relaxation of the Fixed- P_t Formulation:* The fixed- P_t formulation explains why the local solutions become concentrated in Case 2. In the original Case 1 formulation, P_t is derived through u_{psl} , which introduces a strongly nonlinear peak-sidelobe constraint. When the P_t values obtained from Case 1 are fixed and the problem is recalculated, the solutions nearly follow the selected optimal trend of the original formu-

TABLE III
NUMERICAL SETUP AND INPUT PARAMETERS FOR CASE 1.

Frequency [GHz]	Wavelength λ [m]	Inter-satellite distance d_{sat} [m]	Surplus magnetic moment $\bar{\mu}_{\text{mar}}$ [Am ²]	Transmitting power from an element P_t [W]
1	0.30	0.15	0, 0.25, 0.50, 0.75, 1.0	(41) (Calculated for $P_r = -87.2$ dBm and $G_R = 0$ dBi.)

CASE 1: BREAKDOWN OF SIZE, MASS, AND POWER WITH OVERALL SYSTEM MASSES FROM 500 KG TO 6000 KG. IN TERMS OF POWER, ONLY THE SOLAR PANEL GENERATES POWER, WHILE ALL OTHER COMPONENTS CONSUME POWER. THE BUS MASS AND BUS POWER ARE SET AS CONSTANTS AT 200 G AND 200 mW, RESPECTIVELY. THE SLL DENOTES THE NORMALIZED PEAK SIDELobe-ENVELOPE LEVEL RELATIVE TO THE MAIN-BEAM PEAK.

	$\bar{\mu}_{\text{mar}}$ (Am ²)	0			0.25			0.50			0.75			1.0		
		500	3000	6000	500	3000	6000	500	3000	6000	500	3000	6000	500	3000	6000
Overall system mass m_{sys} (kg)		500	3000	6000	500	3000	6000	500	3000	6000	500	3000	6000	500	3000	6000
Size	Satellite $2a_{\text{sat}}$ (mm)	62.7	59.4	61.3	85.0	85.0	85.1	100.0	100.0	100.0	100.0	100.0	100.0	100.0	100.0	100.0
	Coil $2a_{\text{coil}}$ (mm)	40.3	34.9	33.0	75.0	75.0	75.0	75.0	75.0	75.0	75.0	75.0	75.0	75.0	75.0	75.0
	Coil parameter q_{coil} (mm ²)	0.218	0.397	0.356	1.47	1.47	1.47	4.15	4.15	4.15	9.35	9.33	9.33	16.7	16.6	16.6
Mass (g)	Satellite	293	292	292	348	348	348	436	436	436	572	571	571	763	761	761
	3-axis coil	2.33	3.68	3.12	29.3	29.3	29.3	82.7	82.6	82.6	186	186	186	332	330	330
	Battery	9.67	8.69	9.24	17.8	17.8	17.8	24.6	24.6	24.6	24.6	24.6	24.6	24.6	24.6	24.6
	Body	73.2	73.0	73.0	87.0	87.0	87.0	109	109	109	143	143	143	191	190	190
	4 Solar panels	9.43	8.47	9.01	17.3	17.4	17.4	24.0	24.0	24.0	24.0	24.0	24.0	24.0	24.0	24.0
Power (mW)	4 Solar panels ($\times 10^3$)	1.61	1.45	1.54	2.96	2.97	2.97	4.10	4.10	4.10	4.10	4.10	4.10	4.10	4.10	4.10
	Disturbance	683	795	1130	17.8	25.3	27.3	7.43	11.0	11.8	4.00	6.14	6.71	2.74	4.38	4.87
	Transmitter	3.65	0.102	0.0254	5.13	0.143	0.0358	8.03	0.224	0.0561	13.8	0.385	0.0963	24.5	0.683	0.171
	Margin ($\times 10^3$)	0	0	0	2.74	2.74	2.74	3.89	3.89	3.89	3.88	3.89	3.89	3.87	3.87	3.90
Performance	Main-beam EIRP (dBW)	39.5	39.5	39.5	39.5	39.5	39.5	39.4	39.5	39.5	39.4	39.5	39.4	39.5	39.5	39.5
	Maximum antenna gain (dBi)	32.4	40.1	43.1	31.6	39.4	42.4	30.6	38.4	41.4	29.4	37.2	40.3	28.2	36.0	39.0
	Peak SLL envelope (dB)	-13.2	-13.3	-13.3	-13.2	-13.3	-13.3	-13.2	-13.3	-13.3	-13.2	-13.3	-13.3	-13.2	-13.3	-13.3
	Footprint diameter (km)	77.1	31.9	22.6	83.8	34.7	24.6	93.6	38.7	27.5	107	44.3	31.4	123	51.0	36.2
	Satellite number $N_t \times N_l$	41 \times 41	101 \times 101	143 \times 143	39 \times 39	93 \times 93	131 \times 131	35 \times 35	83 \times 83	117 \times 117	29 \times 29	73 \times 73	103 \times 103	25 \times 25	63 \times 63	89 \times 89

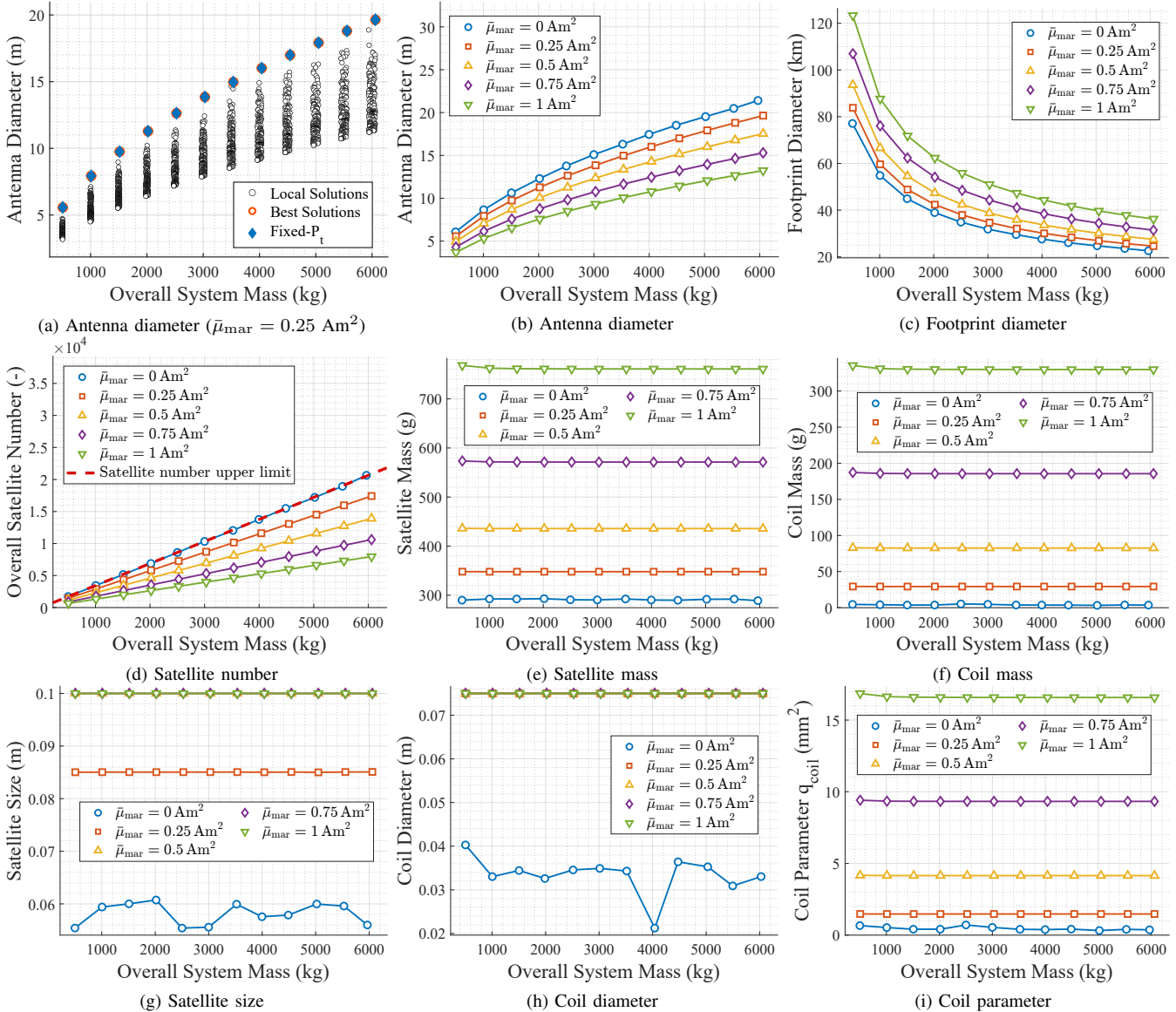


Fig. 5. Representative design solutions for Case 1, where the margin magnetic moment is swept at $\lambda = 0.30$ m and $d_{\text{sat}} = 0.15$ m. Panel (a) compares the original formulation with the fixed- P_t formulation at $\bar{\mu}_{\text{mar}} = 0.25$ Am², showing the scatter of local solutions caused by the peak-sidelobe-related variable. Panels (b)–(i) show the optimal design trends for $\bar{\mu}_{\text{mar}} = 0$ –1.0 Am²; the zero-margin case approaches the satellite-number upper bound with near-minimum satellite mass, whereas nonzero margin magnetic moment reduces the feasible aperture and shifts the coil adjustment toward q_{coil} as the generated-power and satellite-size margins become restrictive.

TABLE V
NUMERICAL SETUP AND INPUT PARAMETERS FOR CASE 2.

Frequency [GHz]	Wavelength λ [m]	Inter-satellite distance d_{sat} [m]	Surplus magnetic moment $\bar{\mu}_{\text{mar}}$ [Am ²]	Transmitting power from an element P_t [W]
1	0.30	0.15	TABLE VI 0.25	[0.1, 0.2, 0.3, 0.4, 0.5]

P_t (W)	0.1			0.2			0.3			0.4			0.5		
	500	3000	6000	500	3000	6000	500	3000	6000	500	3000	6000	500	3000	6000
Overall system mass m_{sys} (kg)	500	3000	6000	500	3000	6000	500	3000	6000	500	3000	6000	500	3000	6000
Size															
Satellite $2a_{\text{sat}}$ (mm)	87.6	87.6	87.6	92.1	92.1	92.2	96.4	96.5	96.5	100.0	100.0	100.0	100.0	100.0	100.0
Coil $2a_{\text{coil}}$ (mm)	75.0	75.0	75.0	75.0	75.0	75.0	75.0	75.0	75.0	75.0	75.0	75.0	75.0	75.0	75.0
Coil parameter q_{coil} (mm ²)	1.56	1.56	1.56	1.56	1.56	1.56	1.56	1.56	1.56	1.58	1.59	1.59	1.82	1.82	1.83
Mass (g)															
Satellite	353	353	353	358	358	358	363	363	363	368	369	369	375	375	375
3-axis coil	30.9	31.0	31.0	30.9	31.0	31.0	30.9	31.0	31.0	31.5	31.6	31.6	36.2	36.3	36.3
Battery	18.9	18.9	18.9	20.9	20.9	20.9	22.9	22.9	22.9	24.6	24.6	24.6	24.6	24.6	24.6
Body	88.2	88.2	88.3	89.5	89.5	89.6	90.8	90.8	90.9	92.1	92.2	92.2	93.7	93.7	93.7
4 Solar panels	18.4	18.4	18.4	20.4	20.4	20.4	22.3	22.3	22.3	24.0	24.0	24.0	24.0	24.0	24.0
Power (mW)															
4 Solar panels ($\times 10^3$)	3.14	3.15	3.15	3.48	3.48	3.48	3.81	3.82	3.82	4.10	4.10	4.10	4.10	4.10	4.10
Disturbance	17.0	24.3	26.1	17.2	24.6	26.4	17.4	24.9	26.8	17.3	24.7	26.6	15.2	21.9	23.5
Transmitter	333	333	333	667	667	667	1000	1000	1000	1330	1330	1330	1670	1670	1670
Margin ($\times 10^3$)	2.59	2.59	2.59	2.59	2.59	2.59	2.59	2.59	2.59	2.55	2.54	2.54	2.22	2.21	2.21
Performance															
Main-beam EIRP (dBW)	53.1	68.7	74.7	56.0	71.6	77.6	57.6	73.2	79.2	58.8	74.3	80.3	59.6	75.1	81.2
Maximum antenna gain (dBi)	31.6	39.3	42.3	31.5	39.3	42.3	31.4	39.2	42.2	31.4	39.1	42.2	31.3	39.1	42.1
Peak SLL envelope (dB)	-13.2	-13.3	-13.3	-13.2	-13.3	-13.3	-13.2	-13.3	-13.3	-13.2	-13.3	-13.3	-13.2	-13.3	-13.3
Footprint Diameter (km)	84.4	34.9	24.8	85.0	35.2	24.9	85.6	35.4	25.1	86.2	35.7	25.3	86.9	36.0	25.5
Satellite number $N_t \times N_r$	37 \times 37	93 \times 93	131 \times 131	37 \times 37	91 \times 91	131 \times 131	37 \times 37	91 \times 91	129 \times 129	37 \times 37	91 \times 91	129 \times 129	37 \times 37	89 \times 89	127 \times 127

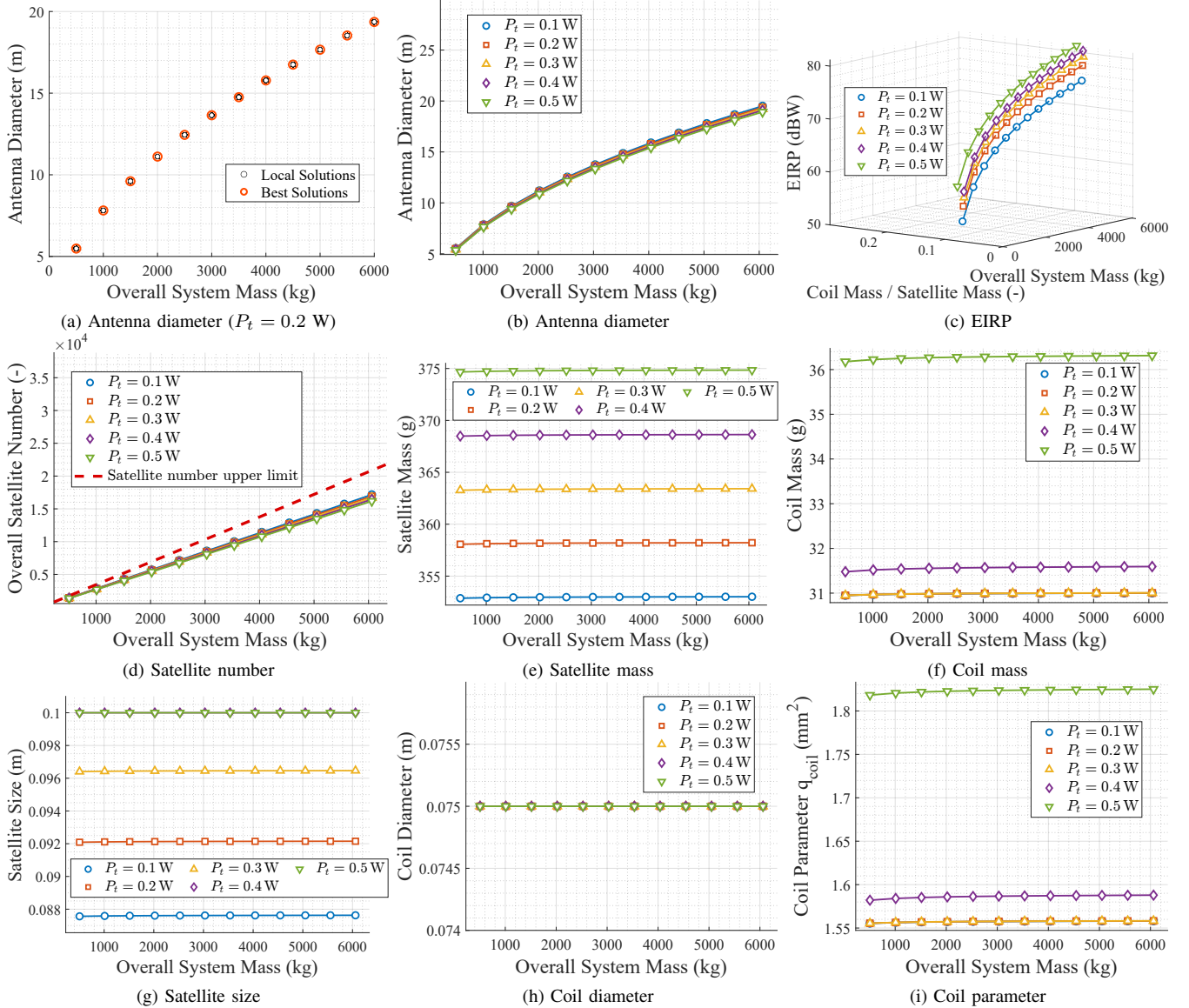


Fig. 6. Representative design solutions for Case 2, where the transmit power is swept at $\lambda = 0.30$ m, $d_{\text{sat}} = 0.15$ m, and $\bar{\mu}_{\text{mar}} = 0.25$ Am². Panel (a) shows the concentrated local-solution trend for the fixed- P_t formulation for $P_t = 0.2$ W. Panels (b)–(i) show that increasing P_t improves EIRP but changes the optimized aperture only moderately; the main design response is an increase in satellite size for solar-power generation, while the coil mass, coil diameter, and coil parameter remain comparatively stable because the EMFF control requirement is fixed.

TABLE VII
NUMERICAL SETUP AND INPUT PARAMETERS FOR CASE 3.

Frequency [MHz]	Wavelength λ [m]	Inter-satellite distance d_{sat} [m]	Surplus magnetic moment $\bar{\mu}_{\text{mar}}$ [Am ²]	Transmitting power from an element P_t [W]
250	1.2	0.60	TABLE VIII 0.25	[0.1, 0.2, 0.3, 0.4, 0.5]

CASE 3: BREAKDOWN OF SIZE, MASS, AND POWER WITH OVERALL SYSTEM MASSES FROM 500 KG TO 6000 KG. IN TERMS OF POWER, ONLY THE SOLAR PANEL GENERATES POWER, WHILE ALL OTHER COMPONENTS CONSUME POWER. THE BUS MASS AND BUS POWER ARE SET AS CONSTANTS AT 200 G AND 200 MW, RESPECTIVELY. THE SLL DENOTES THE NORMALIZED PEAK SIDELobe-ENVELOPE LEVEL RELATIVE TO THE MAIN-BEAM PEAK.

P_t (W)	0.1			0.2			0.3			0.4			0.5		
	500	3000	6000	500	3000	6000	500	3000	6000	500	3000	6000	500	3000	6000
Overall system mass \bar{m}_{sys} (kg)	500	3000	6000	500	3000	6000	500	3000	6000	500	3000	6000	500	3000	6000
Size															
Satellite $2a_{\text{sat}}$ (mm)	100.0	100.0	100.0	100.0	100.0	100.0	100.0	100.0	100.0	100.0	100.0	100.0	100.0	100.0	100.0
Coil $2a_{\text{coil}}$ (mm)	90.0	90.0	90.0	90.0	90.0	90.0	90.0	90.0	90.0	90.0	90.0	90.0	90.0	90.0	90.0
Coil parameter q_{coil} (mm ²)	6.57	12.0	14.3	7.49	14.2	17.4	8.71	17.4	22.1	10.4	22.1	—	12.8	—	—
Mass (g)															
Satellite	533	702	776	562	773	874	601	872	1020	653	1020	—	728	—	—
3-axis coil	157	285	342	179	339	416	208	415	527	248	528	—	305	—	—
Battery	24.6	24.6	24.6	24.6	24.6	24.6	24.6	24.6	24.6	24.6	24.6	—	24.6	—	—
Body	133	176	194	141	193	219	150	218	255	163	255	—	182	—	—
4 Solar panels	24.0	24.0	24.0	24.0	24.0	24.0	24.0	24.0	24.0	24.0	24.0	—	24.0	—	—
Power (mW)															
4 Solar panels ($\times 10^3$)	4.10	4.10	4.10	4.10	4.10	4.10	4.10	4.10	4.10	4.10	4.10	—	4.10	—	—
Disturbance	3210	3370	3400	2920	3070	3100	2630	2770	2800	2340	2460	—	2050	—	—
Transmitter	333	333	333	667	667	667	1000	1000	1000	1330	1330	—	1670	—	—
Margin ($\times 10^3$)	0.356	0.195	0.163	0.312	0.165	0.134	0.268	0.134	0.106	0.225	0.106	—	0.183	—	—
Performance															
Main-beam EIRP (dBW)	49.5	62.7	67.8	52.1	64.9	69.8	53.3	65.6	70.2	53.8	65.5	—	53.8	—	—
Maximum antenna gain (dBi)	29.8	36.3	38.9	29.5	35.9	38.4	29.2	35.4	37.7	28.9	34.7	—	28.4	—	—
Peak SLL envelope (dB)	-13.2	-13.3	-13.3	-13.2	-13.3	-13.3	-13.2	-13.3	-13.3	-13.2	-13.3	—	-13.2	—	—
Footprint Diameter (km)	103	49.1	36.6	106	51.4	38.8	109	54.6	41.9	114	59.0	—	120	—	—
Satellite number $N_i \times N_j$	31 \times 31	65 \times 65	89 \times 89	29 \times 29	63 \times 63	83 \times 83	29 \times 29	59 \times 59	77 \times 77	27 \times 27	55 \times 55	—	27 \times 27	—	—

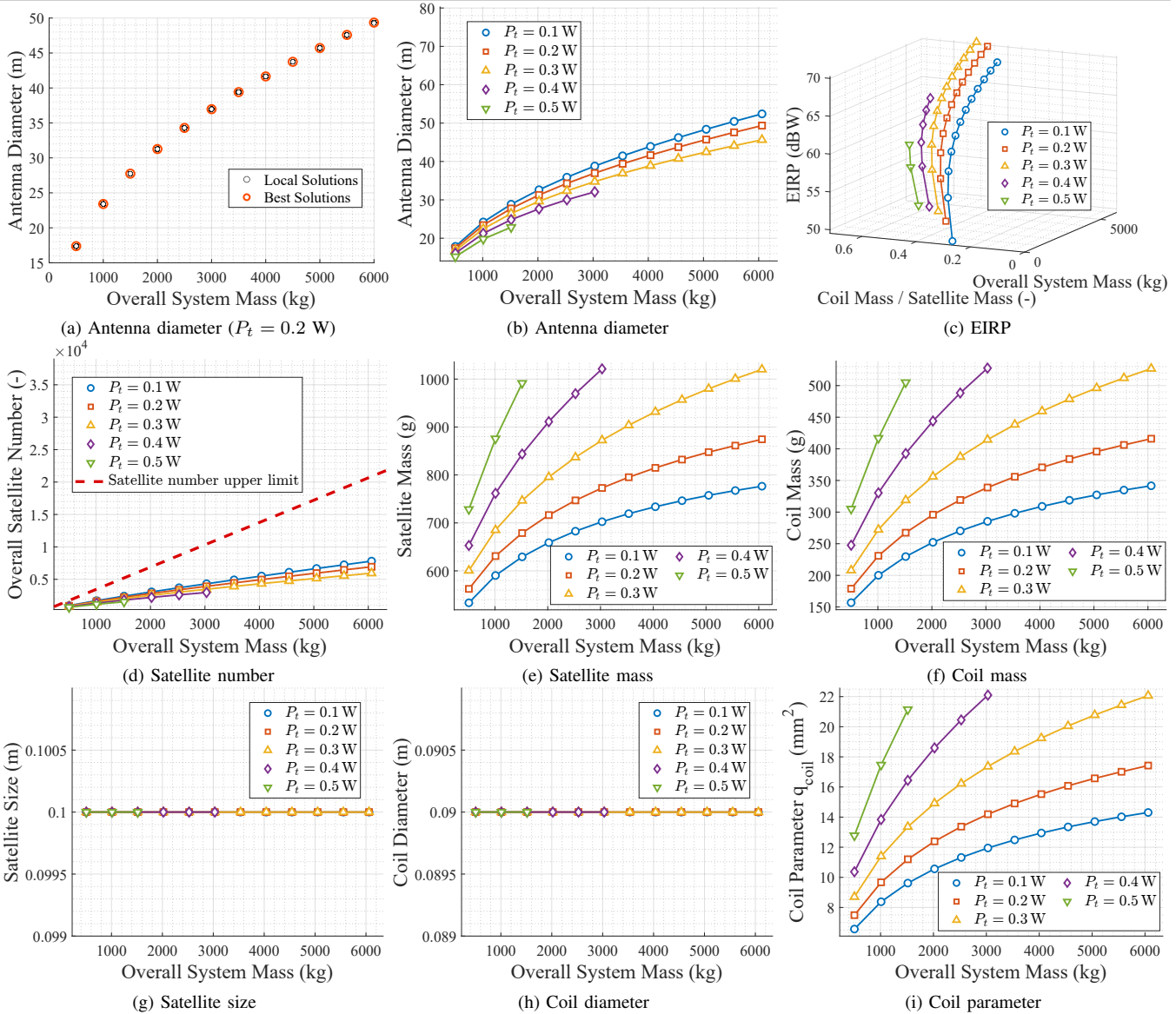


Fig. 7. Representative design solutions for Case 3, where the transmit power is swept under large inter-satellite spacing at $\lambda = 1.20$ m, $d_{\text{sat}} = 0.60$ m, and $\bar{\mu}_{\text{mar}} = 0.25$ Am². The larger spacing increases the geometric aperture but makes EMFF control more demanding. Because the satellite-size margin is nearly exhausted, the coil diameter cannot be enlarged further, and the optimizer increases q_{coil} to reduce coil-related power; this increases the coil and satellite mass, producing infeasible points when the satellite-level mass, size, and power capacities can no longer accommodate the required coil.

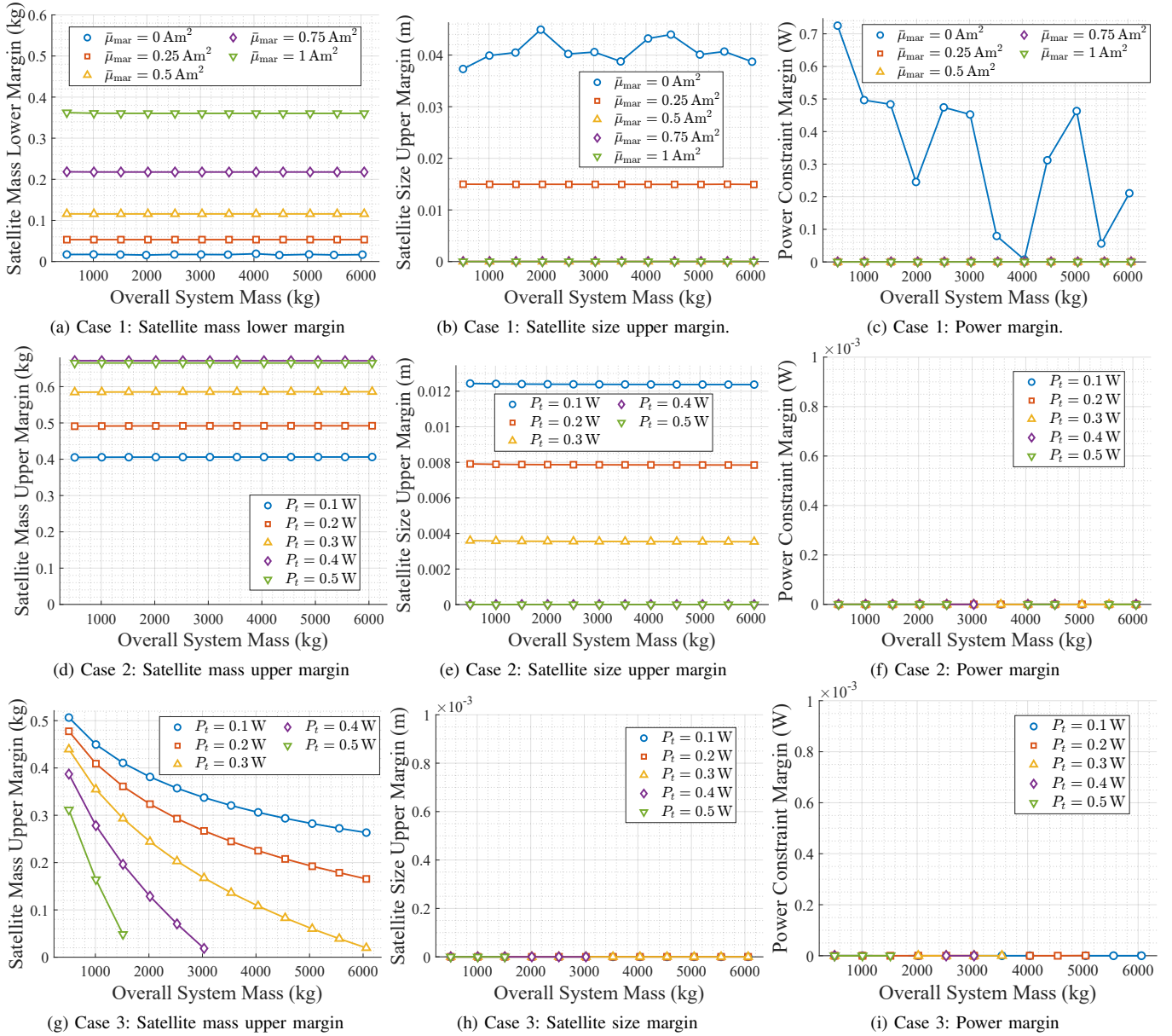


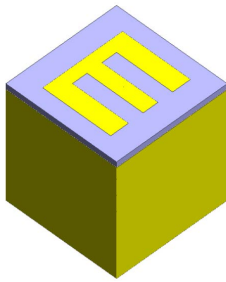
Fig. 8. Constraint margins of satellite mass, satellite size, and power in each case. For satellite mass and satellite size, the active margin with respect to either the upper or lower bound is shown. The power-constraint margin is defined as the generated power from the solar panels minus the total consumed power. The margins indicate how the active bottleneck changes from generated power and satellite size in the baseline-spacing cases to reduced power and size margins with a decreasing satellite-mass upper margin in the large-spacing case.

lation, as shown in Fig. 5a. Case 2 has the same simplified structure because P_t is prescribed, and Fig. 6a shows a concentrated local-solution trend. This behavior indicates that removing u_{psl} leaves a mostly monotonic active-constraint structure, but it does not prove global convexity of the original formulation.

Remark 4. *The original problem is not convex because it includes u_{psl} , integer-like satellite-number sizing, empirical satellite-mass bounds, and a numerically fitted $J_d^*(N_l)$ with negative polynomial coefficients. A relaxed fixed- P_t problem can be written as a geometric program if u_{psl} is removed, N_l is relaxed as a positive continuous variable, m_{sys} is fixed, m_{sat} is eliminated as a dependent posynomial, the total-mass constraint is relaxed to $N_l^2 m_{\text{sat}} \leq m_{\text{sys}}$, the satellite-mass*

bound is replaced by a monomial envelope, and $J_d^(N_l)$ is replaced by a positive-coefficient posynomial upper envelope. Under these relaxations, the problem becomes convex after logarithmic variable transformation [30]. This convexified problem is a conservative relaxation, not a proof of convexity of the original formulation.*

The electromagnetic-field simulation provides a representative check of the no-mutual-coupling antenna model used in the system-level optimization. The proposed framework assumes a simplified array model with idealized antenna elements to keep the satellite-sizing problem tractable. To examine the influence of this assumption, Fig. 9a shows a low-gain antenna element used to approximate the omnidirectional element assumed in the array model, and Fig. 9b shows the



(a) Low-gain antenna element approximating an omnidirectional element

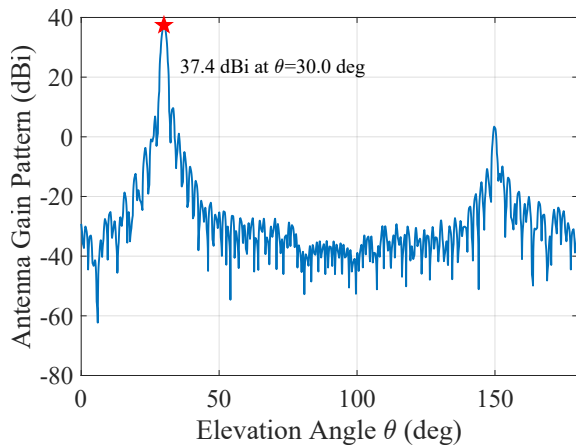
(b) Simulated array gain pattern including mutual coupling for Case 1 with $\bar{\mu}_{\text{mar}} = 0.25 \text{ Am}^2$ and $\bar{m}_{\text{sys}} = 3000 \text{ kg}$

Fig. 9. Electromagnetic-field simulation used to check the effect of mutual coupling on the simplified antenna model. Panel (a) shows the low-gain antenna element used to approximate the omnidirectional element assumed in the system-level array model. Panel (b) shows the radiated gain pattern of the representative Case 1 design with $\bar{\mu}_{\text{mar}} = 0.25 \text{ Am}^2$ and $\bar{m}_{\text{sys}} = 3000 \text{ kg}$, including mutual coupling in the electromagnetic-field simulation.

simulated gain pattern for the representative Case 1 design with $\bar{\mu}_{\text{mar}} = 0.25 \text{ Am}^2$ and $\bar{m}_{\text{sys}} = 3000 \text{ kg}$.

The electromagnetic-field simulation indicates an approximately 2 dB gain reduction relative to the simplified gain model. The antenna gain computed from the no-mutual-coupling approximation in (21) is $G_{\text{model}} = 39.4 \text{ dBi}$, whereas the electromagnetic-field simulation including the element model and mutual coupling gives $G_{\text{EM}} = 37.4 \text{ dBi}$. The difference is therefore $\Delta G = 2.00 \text{ dB}$. This result indicates that the practical element model and mutual coupling reduce the gain, while the simulated value remains close to the value predicted by the simplified model for this representative design. A mutual-coupling-aware radiation model is still required for final antenna design and for evaluating non-uniform or more compact formations.

4) *Design Implications and Future Work:* The proposed framework should be regarded as a design-space analysis framework based on a static grid reference, rather than as a final antenna shape-optimization method. The sizing results in Figs. 5–8 show how the feasible antenna aperture is governed by coupled constraints on satellite mass, size, power, and coil design. Under the assumptions of a uniform square grid, simplified radiation modeling, fixed beam direction, and no mutual-coupling-aware optimization, the framework clarifies

how antenna requirements are translated into satellite designs. These results indicate that the static grid-based EMFF antenna is a useful reference configuration for identifying the dominant bottlenecks in distributed space antenna design under a fixed launch mass.

Future work should extend this reference configuration to more realistic antenna and formation models. Important directions include non-uniform and time-varying formations, relaxed beam-direction constraints, and radiation models that explicitly account for mutual coupling. Dynamic reconfiguration is also important because it requires trajectory optimization that jointly considers orbital motion, design headroom, antenna performance, and control time.

VI. CONCLUSION

This paper proposed a system-level design-space analysis framework for distributed space antennas using electromagnetic formation flight. By linking antenna requirements with satellite-level mass, power, and coil-design constraints, the framework provides a static grid-based reference for designing feasible distributed apertures under a fixed system mass. Unlike our previous bucket-brigade model [28], the formation-maintenance requirement was incorporated through a control index derived from distributed-control simulations. The case studies showed that antenna performance improves with system mass only while satellite-level design headroom remains. In the direct-to-device-oriented case with $d_{\text{sat}} = 0.15 \text{ m}$, generated-power and coil-geometry constraints mainly govern the feasible aperture, whereas the $d_{\text{sat}} = 0.60 \text{ m}$ large-spacing case can become infeasible because the required coil burden exceeds satellite-level mass, size, and power capacities. Future work will extend the framework to non-uniform and time-varying formations, mutual-coupling-aware radiation models, and dynamic reconfiguration with trajectory optimization.

ACKNOWLEDGMENT

The authors used ChatGPT (OpenAI) only to improve language clarity. The tool did not generate the scientific content, results, figures, equations, or references. The authors reviewed and verified all edited text.

REFERENCES

- [1] Y. Takahashi, S. Shim, and S.-i. Sakai, “Distance-based relative orbital transition for palm-sized satellite swarm with guaranteed escape-avoidance,” in *AIAA Scitech 2025 Forum*, 2025, p. 2068.
- [2] Y. Takahashi and S.-I. Sakai, “Graph diffusion-based satellite swarm deployment for curse-of-dimensionality mitigation,” in *AIAA SCITECH 2026 Forum*, 2026, p. 0116.
- [3] Y. Takahashi, A. Ochi, Y. Tomioka, and S.-I. Sakai, “Noda-mmh: Certified learning-aided nonlinear control for magnetically-actuated swarm experiment toward on-orbit proof,” in *International Conference on Space Robotics*. IEEE, 2025.
- [4] D. Tuzi, T. Delamotte, M. Röper, A. Schröder, B. Matthiesen, and A. Knopp, “Multi-beam analysis of satellite swarm-based antenna arrays for 6g direct-to-cell connectivity,” in *2023 IEEE Future Networks World Forum (FNWF)*, 2023.
- [5] C. A. Balanis, *Antenna Theory: Analysis and Design*, 3rd ed. Hoboken, NJ, USA: John Wiley & Sons, 2005.
- [6] Z. N. Chen, D. Liu, H. Nakano, X. Qing, and T. Zwick, Eds., *Handbook of Antenna Technologies*. Singapore: Springer, 2016.

- [7] M. B. Quadrelli, R. Hodges, V. Vilnrotter, S. Bandyopadhyay, F. Tassi, and S. Bevilacqua, "Distributed swarm antenna arrays for deep space applications," in *Proceedings of the 2019 IEEE Aerospace Conference*. IEEE, Mar. 2019, pp. 1–15.
- [8] D. Tuzi, T. Delamotte, and A. Knopp, "Satellite swarm-based antenna arrays for 6g direct-to-cell connectivity," *IEEE Access*, vol. 11, pp. 36 907–36 928, 2023.
- [9] D. You, Y. Takahashi, S. Takeda, M. Moritani, H. Hagiwara, S. Koike, H. Lee, Y. Wang, Z. Li, J. Pang, A. Shirane, H. Sakamoto, and K. Okada, "A ka-band 16-element deployable active phased array transmitter for satellite communication," in *2021 IEEE MTT-S International Microwave Symposium*. IEEE, 2021, pp. 799–802.
- [10] S. Shim, Y. Takahashi, N. Usami, and S. Sakai, "Integrated trajectory and beamforming optimization for fuel-efficient reconfiguration of distributed space antennas," in *AIAA SCITECH 2026 Forum*, 2026, p. 2629.
- [11] Y. She, S. Li, and Z. Wang, "Constructing a large antenna reflector via spacecraft formation flying and reconfiguration control," *Journal of Guidance, Control, and Dynamics*, vol. 42, no. 6, pp. 1372–1382, 2019.
- [12] F. Y. Hadaegh, S.-J. Chung, and H. M. Manohara, "On development of 100-gram-class spacecraft for swarm applications," *IEEE Systems Journal*, vol. 10, no. 2, pp. 673–684, 2014.
- [13] E. M. C. Kong, D. W. Kwon, S. A. Schweighart, L. M. Elias, R. J. Sedwick, and D. W. Miller, "Electromagnetic formation flight for multisatellite arrays," *Journal of Spacecraft and Rockets*, vol. 41, no. 4, pp. 659–666, 2004.
- [14] Y. Takahashi, H. Sakamoto, and S.-i. Sakai, "Kinematics control of electromagnetic formation flight using angular-momentum conservation constraint," *Journal of Guidance, Control, and Dynamics*, vol. 45, no. 2, pp. 280–295, 2022.
- [15] D. J. Barnhart, T. Vladimirova, and M. N. Sweeting, "Very-small-satellite design for distributed space missions," *Journal of Spacecraft and Rockets*, vol. 44, no. 6, pp. 1294–1306, 2007.
- [16] S. A. Schweighart and R. J. Sedwick, "High-fidelity linearized J_2 model for satellite formation flight," *Journal of Guidance, Control, and Dynamics*, vol. 25, no. 6, pp. 1073–1080, 2002.
- [17] C. Craeye and D. González-Ovejero, "A review on array mutual coupling analysis," *Radio Science*, vol. 46, p. RS2012, 2011.
- [18] U. Ahsun, "Dynamics and control of electromagnetic satellite formations," Ph.D. dissertation, Massachusetts Institute of Technology, Aeronautics and Astronautics Department, 2007.
- [19] Y. Takahashi, H. Sakamoto, and S.-i. Sakai, "Simultaneous control of relative position and absolute attitude for electromagnetic spacecraft swarm," in *AIAA Scitech 2021 Forum*, 2021, p. 1104.
- [20] Y. Takahashi and S.-i. Sakai, "Neural power-optimal magnetorquer solution for multi-agent formation and attitude control," *IEEE Robotics and Automation Letters*, 2026.
- [21] S. A. Schweighart, "Electromagnetic formation flight dipole solution planning," Ph.D. dissertation, Massachusetts Institute of Technology, 2005. [Online]. Available: <http://hdl.handle.net/1721.1/32464>
- [22] Y. Takahashi, H. Tajima, and S.-i. Sakai, "Certified coil geometry learning for short-range magnetic actuation and spacecraft docking application," *IEEE Robotics and Automation Letters*, 2026.
- [23] S. Varma and K. D. Kumar, "Multiple satellite formation flying using differential aerodynamic drag," *Journal of Spacecraft and Rockets*, vol. 49, no. 2, pp. 325–336, 2012.
- [24] P. Huang, F. Zhang, L. Chen, Z. Meng, Y. Zhang, Z. Liu, and Y. Hu, "A review of space tether in new applications," *Nonlinear Dynamics*, vol. 94, pp. 1–19, 2018.
- [25] H. Wang, D.-G. Fang, and Y. L. Chow, "Grating lobe reduction in a phased array of limited scanning," *IEEE Transactions on Antennas and Propagation*, vol. 56, no. 6, pp. 1581–1586, 2008.
- [26] Y. Takahashi, S. Shim, H. Sakamoto, and S.-i. Sakai, "Power-efficiency and scalability analysis of magnetically-actuated satellite swarms via convex optimization," *arXiv preprint arXiv:2605.06286*, 2026.
- [27] G. Maral, M. Bousquet, and Z. Sun, *Satellite Communications Systems: Systems, Techniques and Technology*, 5th ed. Chichester, UK: John Wiley & Sons Ltd, 2009.
- [28] S. Shim, Y. Takahashi, N. Usami, M. Kubota, and S.-i. Sakai, "Feasibility study of distributed space antennas using electromagnetic formation flight," in *2025 IEEE Aerospace Conference*. IEEE, 2025, pp. 1–18.
- [29] Y. Takahashi and S. Shin-Ichiro, "Scalable satellite swarm deployment via distance-based orbital transition under j_2 perturbation," *arXiv preprint*, 2025.
- [30] S. P. Boyd and L. Vandenberghe, *Convex Optimization*. Cambridge University Press, 2004.
- [31] Y. T. Lo and S. Lee, *Antenna Handbook: theory, applications, and design*. Springer Science & Business Media, 2013.
- [32] E. Gilbert and S. Morgan, "Optimum design of directive antenna arrays subject to random variations," *Bell System Technical Journal*, vol. 34, no. 3, pp. 637–663, 1955.
- [33] D. J. Barnhart, T. Vladimirova, A. M. Baker, and M. N. Sweeting, "A low-cost femtosatellite to enable distributed space missions," *Acta Astronautica*, vol. 64, no. 11–12, pp. 1123–1143, 2009.
- [34] S. Bryan and K. Kumar, "Ryefemsat: Ryerson university femtosatellite design and testing," in *SpaceOps 2010 Conference Delivering on the Dream Hosted by NASA Marshall Space Flight Center and Organized by AIAA*. American Institute of Aeronautics and Astronautics, 2010, p. 2157.
- [35] Z. Hu, T. Timmons, L. Stamat, and C. McInnes, "Development of a 10g femtosatellite with active attitude control," in *17th Reinventing Space Conference, Belfast, Northern Ireland*, 2019.
- [36] J. Cao, C. Clemente, C. McInnes, J. Soraghan, and D. Uttamchandani, "A novel concept for earth remote sensing using a bistatic femto-satellite swarm in sun synchronous orbit," in *66th International Astronautical Congress, Jerusalem, Israel*, 2015.
- [37] J. Liesen and Z. Strakos, *Krylov Subspace Methods: Principles and Analysis*. Numerical Mathematics and Scie, 2013.
- [38] Y.-W. Liu, D.-J. Zhang, P.-C. Tsai, C.-T. Chiang, W.-C. Tu, and S.-Y. Lin, "Nanometer-thick copper films with low resistivity grown on 2d material surfaces," *Scientific Reports*, vol. 12, p. 1823, 2022.
- [39] W. M. Haynes, Ed., *CRC Handbook of Chemistry and Physics*, 95th ed. Boca Raton, FL: Taylor & Francis Group, 2014.
- [40] 3rd Generation Partnership Project (3GPP), "5G; NR; User Equipment (UE) Radio Transmission and Reception; Part 1: Range 1 Standalone," 3GPP, Technical Specification (TS) 38.101-1, Aug. 2022.
- [41] I. The MathWorks, *GlobalSearch - MATLAB & Simulink*, MathWorks, accessed: May 17, 2026.